

1 **SUPPORTING INFORMATION**

2 **Quasi-Double-Star Nickel and Iron Active Sites for High-Efficient Carbon
3 Dioxide Electroreduction**

4 Ting Zhang,^{a,b} Xu Han,^a Hong Liu,^c Martí Biset-Peiró,^b Xuan Zhang,^{d,e} Pingping
5 Tan,^e Pengyi Tang,^{*f,g} Bo Yang,^c Lirong Zheng,^{*h} Joan Ramon Morante,^{b,i} Jordi
6 Arbiol^{*a,j}

7 ^aCatalan Institute of Nanoscience and Nanotechnology (ICN2), CSIC and BIST, Campus UAB,
8 Bellaterra, Barcelona, 08193, Catalonia, Spain

9 ^bCatalonia Institute for Energy Research (IREC), Jardins de les Dones de Negre 1, Sant Adrià del
10 Besòs, Barcelona, 08930, Catalonia, Spain

11 ^cSchool of Physical Science and Technology, ShanghaiTech University, 393 Middle Huaxia Road,
12 Shanghai, 201210, P. R. China

13 ^dDepartment of Materials Engineering, KU Leuven, Kasteelpark Arenberg, 44, B-3001 Leuven,
14 Belgium

15 ^eInstitute for Clean Energy & Advanced Materials, Faculty of Materials & Energy, Southwest
16 University, Chongqing 400715, China.

17 ^fErnst Ruska-Centre for Microscopy and Spectroscopy with Electrons and Peter Grünberg Institute,
18 Forschungszentrum Jülich GmbH, Jülich, 52425, Germany

19 ^gInstitute of Microsystem and Information Technology, Chinese Academy of Sciences, Shanghai,
20 200050, P. R. China

21 ^hBeijing Synchrotron Radiation Facility, Institute of High Energy Physics, Chinese Academy of
22 Sciences, Beijing, 100049, P. R. China

23 ⁱDepartment of Physics, Universitat de Barcelona, Barcelona, 08028, Catalonia, Spain

24 ^jICREA, Pg. Lluís Companys 23, Barcelona, 08010, Catalonia, Spain

25 *Correspondence: py.tang@mail.sim.ac.cn (P.T)

26 *Correspondence: zhenglr@ihep.ac.cn (L.Z)

27 *Correspondence: arbiol@icrea.cat (J.A)

28

29

30

31

32

33

1 CONTENTS

2	Materials and Characterization.....	5
3	Materials	5
4	Characterization	5
5	XAFS Measurements	7
6	XAFS Analysis and Results	7
7	Ink Preparation	8
8	Electrochemical Measurement	9
9	Calculation Method	11
10	DFT Calculations	12
11	Figure S1. XRD patterns of Ni-IRMOF-3, Fe-IRMOF-3 and Ni ₇ /Fe ₃ -IRMOF-3	14
12	Figure S2. FTIR spectrum of IRMOF-3, Ni-IRMOF-3, Fe-IRMOF-3 and	
13	Ni ₇ /Fe ₃ -IRMOF-3	15
14	Figure S3. SEM images of IRMOF-3, Ni-IRMOF-3, Fe-IRMOF-3, Ni ₇ /Fe ₃ -IRMOF-3	
15	16
16	Figure S4. HAADF STEM image of Ni-IRMOF-3 and representative EELS chemical	
17	composition maps	17
18	Figure S5. HAADF STEM image of Fe-IRMOF-3 and representative EELS chemical	
19	composition maps	17
20	Figure S6. BF TEM, HAADF STEM image of Ni ₇ /Fe ₃ -IRMOF-3 and representative	
21	EELS chemical composition maps obtained from the red squared area of the STEM	
22	micrograph.	18
23	Figure S7. N ₂ adsorption and desorption isotherm and BET surface areas for	
24	IRMOF-3, Ni-IRMOF-3, Fe-IRMOF-3 and Ni ₇ /Fe ₃ -IRMOF-3	19
25	Figure S8. TGA patterns of Ni ₇ /Fe ₃ -IRMOF-3	20
26	Table S1. Ni and Fe loading ratios of different samples	20
27	Figure S9. XRD patterns of Ni-N-C and Fe-N-C	21
28	Figure S10. Raman spectra of Ni-N-C and Fe-N-C	22
29	Figure S11. Low magnification and high magnification aberration-corrected HAADF	
30	STEM images of Ni ₇ /Fe ₃ -N-C sample	23
31	Figure S12. HAADF STEM image of Ni ₇ /Fe ₃ -N-C and representative EDX chemical	
32	composition maps	24
33	Figure S13. HAADF STEM, BF TEM images of Ni-N-C, HAADF STEM image and	
34	representative EELS chemical composition maps obtained from the red squared area	
35	of the STEM micrograph	25
36	Figure S14. HAADF STEM, BF TEM, HRTEM images of Fe-N-C as well as	
37	HAADF STEM image and representative EELS chemical composition maps obtained	
38	from the red squared area of the STEM micrograph	26
39	Figure S15. CV curves of Ni-N-C, Fe-N-C and Ni ₇ /Fe ₃ -N-C in 0.5 M NaHCO ₃	
40	electrolyte	27
41	Figure S16. XPS survey spectra of Ni-N-C and Fe-N-C	28

Figure S17. High-resolution XPS N 1s of Ni-N-C and Fe-N-C	28
Figure S18. High-resolution XPS O 1s of Ni-N-C and Fe-N-C	28
Figure S19. The enlarged pre-edge region of Ni K-edge XANES spectra and Fe K-edge XANES spectra.....	29
Figure S20. The corresponding Fe K-edge EXAFS fitting parameters for Fe-N-C and Ni ₇ /Fe ₃ -N-C samples.	30
Table S2. EXAFS fitting parameters at the Ni K-edge for various samples	30
Table S3. EXAFS fitting parameters at the Fe K-edge for various samples	30
Figure S21. The representative ¹ H-NMR spectra of the electrolyte after electrolysis of −0.50 V for Ni ₇ /Fe ₃ -N-C in CO ₂ -saturated 0.5 M NaHCO ₃ electrolyte for 30 h.	31
Figure S22. LSV curves vs. RHE of Ni-IRMOF-3, Fe-IRMOF-3 and Ni ₇ /Fe ₃ -IRMOF-3 obtained in Ar- or CO ₂ -saturated 0.5 M NaHCO ₃ solution. FE of CO at various potentials and FE of H ₂ at various potentials on Ni-IRMOF-3, Fe-IRMOF-3, Ni ₇ /Fe ₃ -IRMOF-3.....	32
Figure S23. CV curves vs. RHE of Ni-N-C, Fe-N-C, Ni ₇ /Fe ₃ -N-C and LSV curves vs. RHE of Ni ₇ /Fe ₃ -N-C obtained in Ar- or CO ₂ -saturated 0.5 M NaHCO ₃ solution.....	33
Figure S24. TOF value of different samples	34
Figure S25. Cyclic voltammograms curves for Ni-IRMOF-3, Fe-IRMOF-3, Ni ₇ /Fe ₃ -IRMOF-3, Ni-N-C, Fe-N-C and Ni ₇ /Fe ₃ -N-C. Plots of the current density vs. scan rate for Ni-IRMOF-3, Fe-IRMOF-3, Ni ₇ /Fe ₃ -IRMOF-3, Ni-Ni-N-C, Fe-N-C and Ni ₇ /Fe ₃ -N-C electrodes	35
Figure S26. Linear sweep voltammetry curves of Ni-N-C, Fe-N-C and Ni ₇ /Fe ₃ -N-C with and without 0.05 M NaSCN.	36
Figure S27. Electrochemical impedance spectroscopy (EIS) of Ni-IRMOF-3, Fe-IRMOF-3, Ni ₇ /Fe ₃ -IRMOF-3, Ni-N-C, Fe-N-C and Ni ₇ /Fe-N-C.....	37
Figure S28. Current density and FE of Ni ₇ /Fe-N-C at different NaHCO ₃ concentration at a constant potential (−0.50 V vs. RHE). Partial CO current density of Ni ₇ /Fe ₃ -N-C vs. NaHCO ₃ concentration at −0.50 V vs. RHE	38
Figure S29. FE of CO and FE of H ₂ at various potentials on Ni _x /Fe ₇ -N-C	39
Figure S30. FE of CO and FE of H ₂ at various potentials on Ni ₇ /Fe ₃ -N-C and Ni ₇ /Co ₃ -N-C.....	40
Figure S31. FE of CO at various potentials and Current density for CO production on Ni ₇ /Fe ₃ -N-C and Ni ₇ /Fe ₃ -N-C-P.....	40
Figure S32. XRD patterns and FTIR image of 2-Ni ₇ /Fe ₃ -IRMOF-3.....	41
Figure S33. SEM images of 2-Ni ₇ /Fe ₃ -IRMOF-3	41
Figure S34. BF TEM, HAADF STEM image of 2-Ni ₇ /Fe ₃ -IRMOF-3 and representative EELS chemical composition maps obtained from the red squared area of the STEM micrograph	42
Figure S35. TGA of 2-Ni ₇ /Fe ₃ -IRMOF-3	43
Figure S36. XRD patterns and Raman spectra of 2-Ni ₇ /Fe ₃ -N-C.....	44
Figure S37. HAADF STEM, BF TEM images of 2-Ni ₇ /Fe ₃ -N-C, HAADF STEM image and representative EELS chemical composition maps obtained from the red squared area of the STEM micrograph	45
Figure S38. XPS spectra for the survey scan, C 1s, N 1s and O 1s of 2-Ni ₇ /Fe ₃ -N-C.	

1	46
2	Figure S39. Ni K-edge XANES spectra of Ni foil and 2-Ni ₇ /Fe ₃ -N-C. Fe K-edge	
3	XANES spectra of Fe foil and 2-Ni ₇ /Fe ₃ -N-C. Fourier transformation of the EXAFS	
4	spectra at R space.....	47
5	Figure S40. LSV and CV curves vs. RHE of 2-Ni ₇ /Fe ₃ -N-C obtained in Ar- or	
6	CO ₂ -saturated 0.5 M NaHCO ₃ solution. FE of CO and FE of H ₂ at various potentials	
7	on Ni ₇ /Fe ₃ -N-C and 2-Ni ₇ /Fe ₃ -N-C	48
8	Figure S41. Linear sweep voltammetry curves of 2-Ni ₇ /Fe ₃ -N-C with and without	
9	0.05 M NaSCN.....	49
10	Figure S42. The top view and side view of optimized adsorption configuration on	
11	simulated models	50
12	Table S4. Faradaic Efficiency (CO) of the reported single/double atom-based	
13	electrocatalysts for CO ₂ electroreduction	51
14	References	52
15		
16		
17		
18		
19		
20		
21		
22		
23		
24		
25		
26		
27		
28		
29		
30		
31		
32		
33		
34		

1 **Materials and Methods**

2 **Materials:**

3 If not specified, all chemical reagents were purchased from Sigma-Aldrich. Zinc
4 nitrate hexahydrate ($\text{Zn}(\text{NO}_3)_2 \cdot 6\text{H}_2\text{O}$), 2-Aminoterphthalic acid, iron chloride
5 hexahydrate ($\text{FeCl}_3 \cdot 6\text{H}_2\text{O}$), cobaltous nitrate hexahydrate ($\text{Co}(\text{NO}_3)_2 \cdot 6\text{H}_2\text{O}$), nickel
6 chloride hexahydrate ($\text{NiCl}_2 \cdot 6\text{H}_2\text{O}$), N,N-dimethylformamide (DMF), sodium
7 thiocyanate (NaSCN), ethanol and sodium bicarbonate (NaHCO_3) were all of
8 analytical grade and used as received without further purification. Meanwhile, all
9 solutions were prepared with Milli-Q water (DI- H_2O , Ricca Chemical, ASTM Type I).

10 The carbon paper was purchased from Alfa Aesar. The Nafion (N-117 membrane,
11 0.18 mm thick) was also purchased from Alfa Aesar and kept in 0.5 M NaOH
12 solution.

13 **Characterization:**

14 The X-ray diffraction patterns (XRD) were obtained through a Bruker D4 X-ray
15 powder diffractometer using Cu K α radiation (1.54184 Å). Field emission scanning
16 electron microscopy (FESEM) images were collected on a FEI Magellan 400 L
17 scanning electron microscope. The transmission electron microscopy (TEM) and high
18 angle annular dark field scanning TEM (HAADF STEM) images were obtained in a
19 Tecnai F20 field emission gun microscope with a 0.19 nm point-to-point resolution at
20 200 kV equipped with an embedded Quantum Gatan Image Filter for EELS analyses.
21 Images have been analyzed by means of Gatan Digital Micrograph software. Parts of
22 HAADF-STEM images and elemental mapping (EDX) were obtained in a spherical

1 aberration-corrected (AC) transmission electron microscope FEI Themis Z and
2 operated at 200 kV. X-ray photoelectron spectroscopy (XPS) was performed on a
3 Phoibos 150 analyser (SPECS GmbH, Berlin, Germany) in ultra-high vacuum
4 conditions (base pressure 4×10^{-10} mbar) with a monochromatic aluminum K α X-ray
5 source (1486.74 eV). Binding energies (BE) were determined using the C 1s peak at
6 284.5 eV as a charge reference. Inductively coupled plasma-mass spectrometry
7 (ICP-MS) measurements were carried out to determine the concentration of Fe.
8 Brunauer-Emmett-Teller (BET) surface areas were measured using nitrogen
9 adsorption at 77 K. Raman spectra were obtained using Senterra. Fourier transformed
10 infrared (FTIR) spectroscopy data were recorded on an Alpha Bruker spectrometer.
11 Thermogravimetric Analysis was measured by Pyris 1 TGA, Perkin Elmer.

12

13

14

15

16

17

18

19

20

21

22

1 **XAFS Measurements:**

2 The X-ray absorption fine structure spectra (Fe K-edge) were collected at 1W1B
3 station in Beijing Synchrotron Radiation Facility (BSRF). The storage rings of BSRF
4 were operated at 2.5 GeV with an average current of 250 mA. Using Si(111)
5 double-crystal monochromator, the data collection were carried out in
6 transmission/fluorescence mode using ionization chamber. All spectra were collected
7 in ambient conditions.

8 **XAFS Analysis and Results:**

9 The acquired EXAFS data were processed according to the standard procedures using
10 the ATHENA module implemented in the IFEFFIT software packages. The
11 k^3 -weighted EXAFS spectra were obtained by subtracting the post-edge background
12 from the overall absorption and then normalizing with respect to the edge-jump step.
13 Subsequently, k^3 -weighted $\chi(k)$ data of Fe K-edge were Fourier transformed to real (R)
14 space using a hanning windows ($dk=1.0 \text{ \AA}^{-1}$) to separate the EXAFS contributions
15 from different coordination shells. To obtain the quantitative structural parameters
16 around central atoms, least-squares curve parameter fitting was performed using the
17 ARTEMIS module of IFEFFIT software packages.¹⁻³

18

19

20

21

22

1 **Ink Preparation:**

2 2 mg synthesized different samples and 50 μ l 5 wt% Nafion solutions were dissolved
3 in ethanol (1 ml) and ultrasonicated for 1 h to form evenly suspension for the further
4 electrochemical experiments. To prepare the working electrode, 500 μ L above
5 as-prepared inks were dropped onto the two sides of the carbon paper electrode with
6 1×1 cm² and then dried at room temperature for a few minutes, giving a catalyst
7 loading mass of \sim 1 mg cm⁻².

8

9

10

11

12

13

14

15

16

17

18

19

20

21

22

1 **Electrochemical Measurement:**

2 The electrocatalytic performance of different catalysts was measured at room
3 temperature by using a gas-tight H-cell with two-compartments separated by a cation
4 exchange membrane (Nafion N-117 membrane) with a continuously Ar or CO₂ gas
5 injection. Each compartment contained 70 ml electrolyte (0.5 M NaHCO₃ made from
6 de-ionized water). In a typical experiment, a standard three electrode setup in 0.5 M
7 NaHCO₃ solution was assembled: an Ag/AgCl electrode as a reference electrode, a Pt
8 plate as a counter electrode and a carbon paper coated with the different samples as a
9 working electrode (surface area = 1 cm²). The potentials were measured versus
10 Ag/AgCl and converted to the reversible hydrogen electrode (RHE) according to the
11 following equation: E_{RHE} = E⁰_{Ag/AgCl} + E_{Ag/AgCl} + 0.059 × pH, pH=7.⁴ All
12 electrochemical results were showed without iR-compensation by using a
13 computer-controlled BioLogic VMP3 electrochemical workstation. Meanwhile, the
14 linear sweep voltammetry (LSV) was performed at a scan rate of 20 mV s⁻¹ from 0 V
15 to -1.5 V vs. Ag/AgCl in Ar-saturated 0.5 M NaHCO₃ (pH=8.5) and CO₂-saturated
16 0.5 M NaHCO₃ (pH=7) as supporting electrolyte. The cyclic voltammetry (CV) was
17 performed at a scan rate of 20 mV s⁻¹. Moreover, electrochemical impedance
18 spectroscopy (EIS) of different samples was carried out in a frequency range from 100
19 kHz to 100 mHz.

20 Before the electrochemical CO₂ reduction experiments, an average rate of 20 ml
21 min⁻¹ Ar was injected into cathodic electrolyte in order to form an Ar-saturated
22 solution. During electrochemical CO₂ reduction experiments, the CO₂ gas was

1 delivered at an average rate of 20 ml min⁻¹ at room temperature and ambient pressure,
2 measured downstream by a volumetric digital flowmeter. The gas phase composition
3 was analyzed by gas chromatography (GC) during potentiostatic measurements every
4 20 min. The calibration of peak area vs. gas concentration was used for the molar
5 quantification of each gaseous effluent. The Faradaic efficiency was calculated by
6 determining the number of coulombs needed for each product and then dividing by
7 the total charge passed during the time of the GC sampling according to the flow rate.
8 Liquid products were analyzed afterwards by quantitative ¹H-NMR using water as the
9 deuterated solvent.

10

11

12

13

14

15

16

17

18

19

20

21

22

1 **Calculation Method:**

2 Details concerning the Faradaic Efficiency (FE) calculations are shown below.⁴⁻⁷

3 The partial current density for a given gas product was calculated as below:

4
$$j_i = x_i \times V \times \frac{n_i F P_0}{RT} \times (\text{electrode area})^{-1}$$

5 Where x_i is the volume fraction of a certain product determined by online GC

6 referenced to calibration curves from three standard gas samples, V is the flow rate, n_i

7 is the number of electrons involved, $P_0 = 101.3$ kPa, F is the Faraday constant, and R

8 is the gas constant. The corresponding FE at each potential is calculated by

9
$$FE = \frac{j_i}{j} \times 100\%$$

10 TOF for CO production was calculated as follow equation:

11
$$TOF = \frac{(I_{\text{product}}/nF)}{(m_{\text{cat}} \times \omega/M_{\text{metal}})} \times 3600$$

12 Where I_{product} is partial current for certain product, A, n=2, the number of electrons

13 transferred for CO production, F is the Faraday constant, 96485 C mol⁻¹, m_{cat} is the

14 mass of catalyst on the carbon paper, g. ω is the metal loading in the catalyst, and

15 M_{metal} is atomic mass of Ni (58.69 g mol⁻¹) for Ni-N-C, atomic mass of Fe (55.85 g

16 mol⁻¹) for Fe-N-C, and atomic mass of 56.99 g mol⁻¹ for Ni₇/Fe₃-N-C (based on the

17 ratio of Ni and Fe).

18

19

20

21

22

23

24

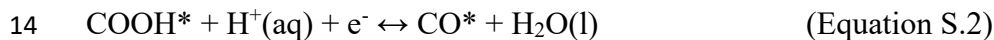
25

26

27

DFT Calculations:

The spin-polarized DFT calculations with projector augmented wave (PAW) method⁸⁻¹¹ were performed using the Vienna ab initio Simulation Package (VASP) code.¹² The Bayesian error estimation functional with van der Waals correlation (BEEF-vdW) was employed to set the plane wave basis.¹³ The convergence criteria were 0.05 eV/ Å in force and 1×10^{-4} eV in energy and the plane wave cutoff was 500 eV. The Monkhorst–Pack mesh k-point grids were $2 \times 2 \times 1$ for all models. All the vacuum thicknesses were higher than 15 Å. With the BEEF-vdW function, the energy of the gas phase molecules gave a systematic correction by +0.41 and +0.09 eV for gaseous CO₂ and H₂, respectively.¹⁴⁻¹⁶ For the electroreduction of CO₂ to CO, the following elementary steps were considered:



16 where (g), (aq) represent the gaseous phase and aqueous phase, respectively. The *,
 17 COOH* and CO* represent free site, adsorption state of COOH and CO, respectively.

18 The reaction free energies of each step was calculated by the following formula:

$$19 \quad G = E_{\text{DFT}} + E_{\text{ZPE}} + \int C_p dT - TS + E_{\text{sol}} \quad (\text{Equation S.4})$$

20 the E_{DFT} is the DFT calculated energy, E_{ZPE} is the zero-point energy, C_p is the
 21 constant pressure heat capacity, T is temperature, S is the entropy. The E_{sol} is solvation
 22 correction, which is -0.1 eV for CO* and -0.25 eV COOH*.¹⁷ The temperature for the

1 reaction is considered as 298.15 K here.

2

3

4

5

6

7

8

9

10

11

12

13

14

15

16

17

18

19

20

21

22

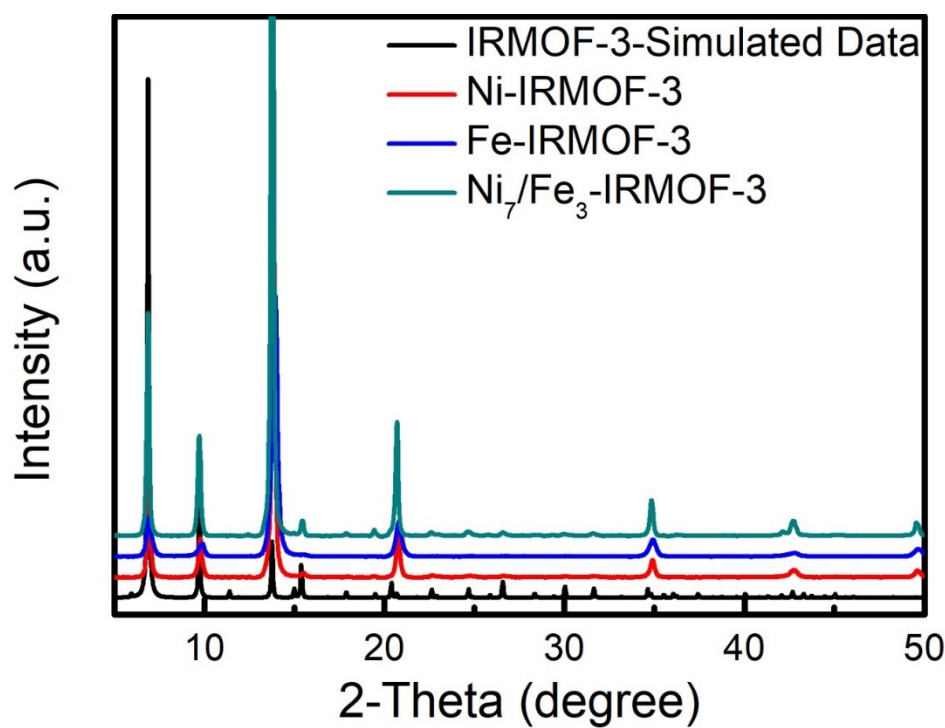


Fig. S1. XRD patterns of Ni-IRMOF-3, Fe-IRMOF-3 and Ni₇/Fe₃-IRMOF-3.

10
11
12
13
14
15
16
17
18
19
20
21
22
23
24
25
26
27
28
29
30
31
32
33
34
35

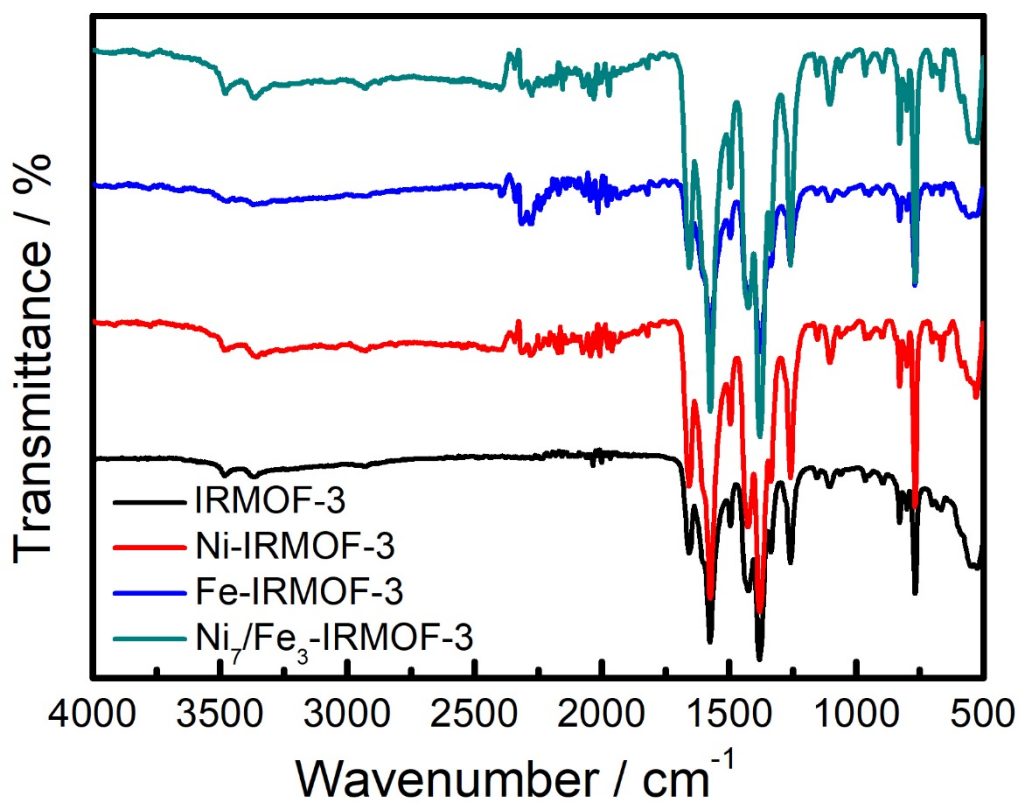
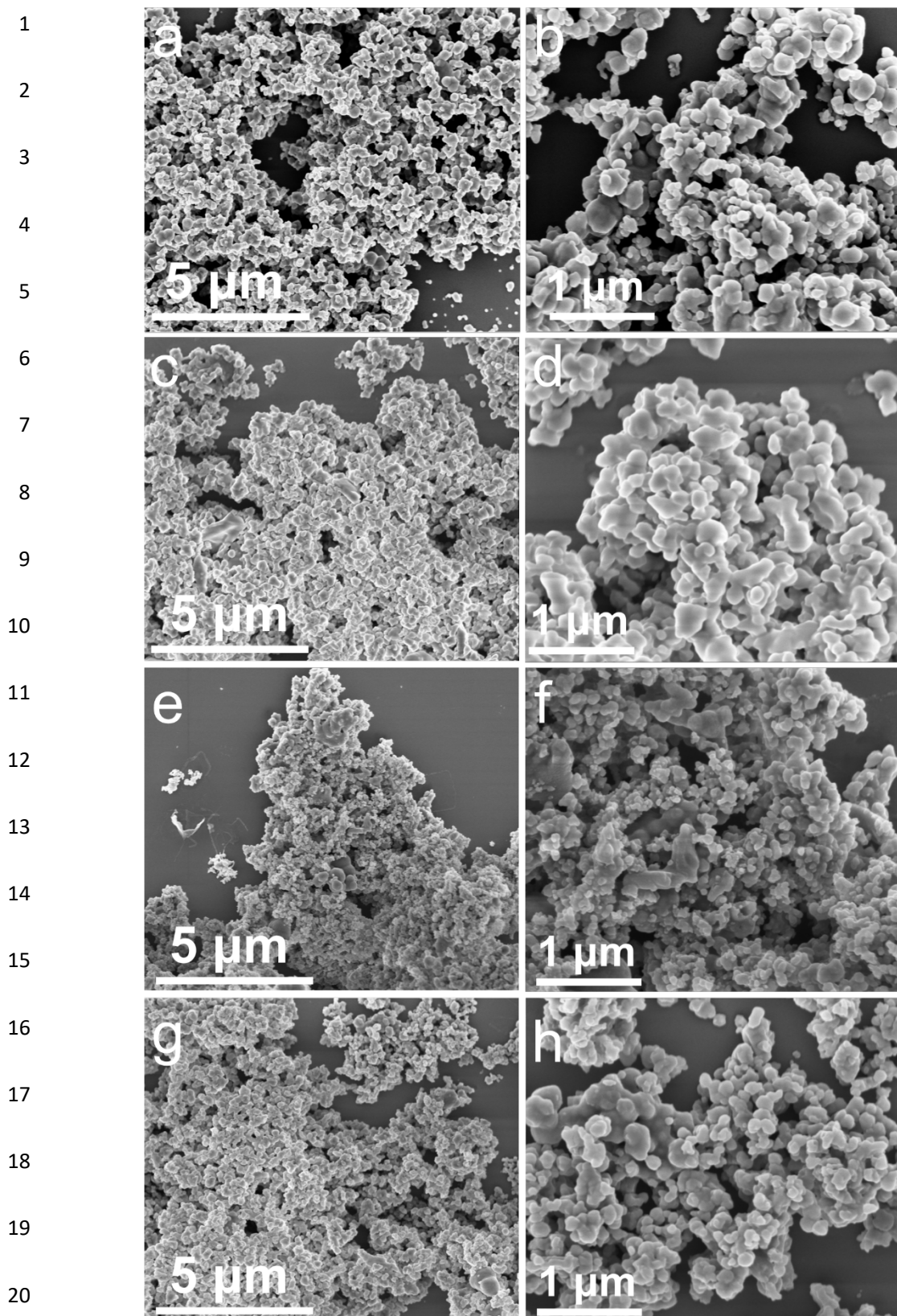
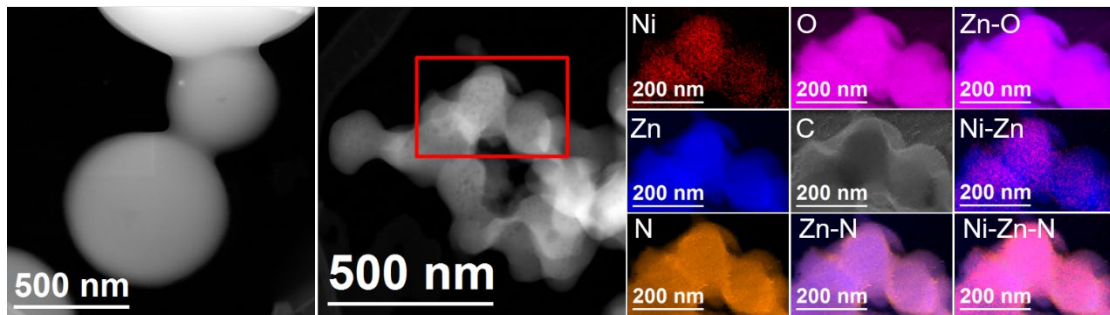


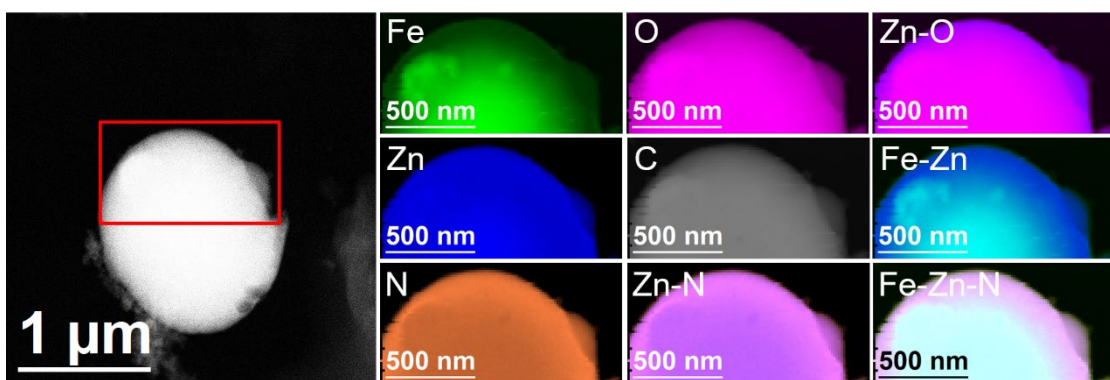
Fig. S2. FTIR spectrum of IRMOF-3, Ni-IRMOF-3, Fe-IRMOF-3 and Ni_7/Fe_3 -IRMOF-3.



21 **Fig. S3.** SEM images of (a and b) IRMOF-3, (c and d) Ni-IRMOF-3, (e and f) Fe-IRMOF-3, (g
22 and h) Ni₇/Fe₃-IRMOF-3.
23
24



9 Fig. S4. HAADF STEM image of Ni-IRMOF-3 and representative EELS chemical composition
10 maps obtained from the red squared area of the STEM micrograph. Individual Ni L_{2,3}-edges at 855
11 eV (red), Zn L_{2,3}-edges at 1020 eV (blue), N K-edges at 401 eV (orange), O K-edges at 532 eV
12 (pink) and C K-edges at 285 eV (grey) as well as composites of Zn-N, Zn-O, Ni-Zn and Ni-Zn-N.



23 Fig. S5. HAADF STEM image of Fe-IRMOF-3 and representative EELS chemical composition
24 maps obtained from the red squared area of the STEM micrograph. Individual Fe L_{2,3}-edges at 708
25 eV (green), Zn L_{2,3}-edges at 1020 eV (blue), N K-edges at 401 eV (orange), O K-edges at 532 eV
26 (pink) and C K-edges at 285 eV (grey) as well as composites of Zn-N, Zn-O, Fe-Zn and Fe-Zn-N.

27
28
29
30
31
32
33
34
35
36
37
38
39
40
41
42
43
44

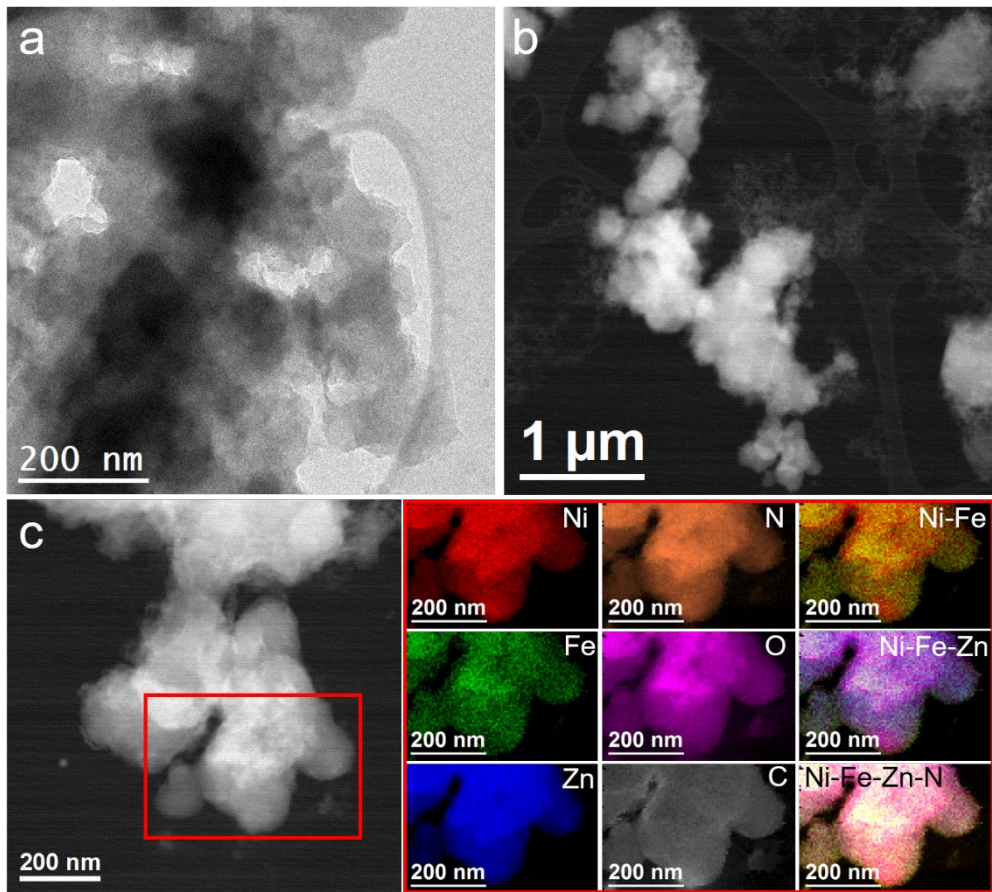


Fig. S6. (a) BF TEM, (b, c) HAADF STEM image of $\text{Ni}_7/\text{Fe}_3\text{-IRMOF-3}$ and representative EELS chemical composition maps obtained from the red squared area of the STEM micrograph. Individual $\text{Ni L}_{2,3}\text{-edges}$ at 855 eV (red), $\text{Fe L}_{2,3}\text{-edges}$ at 708 eV (green), $\text{Zn L}_{2,3}\text{-edges}$ at 1020 eV (blue), $\text{N K}\text{-edges}$ at 401 eV (orange), $\text{O K}\text{-edges}$ at 532 eV (pink) and $\text{C K}\text{-edges}$ at 285 eV (grey) as well as composites of Ni-Fe , Ni-Fe-Zn and Ni-Fe-Zn-N .

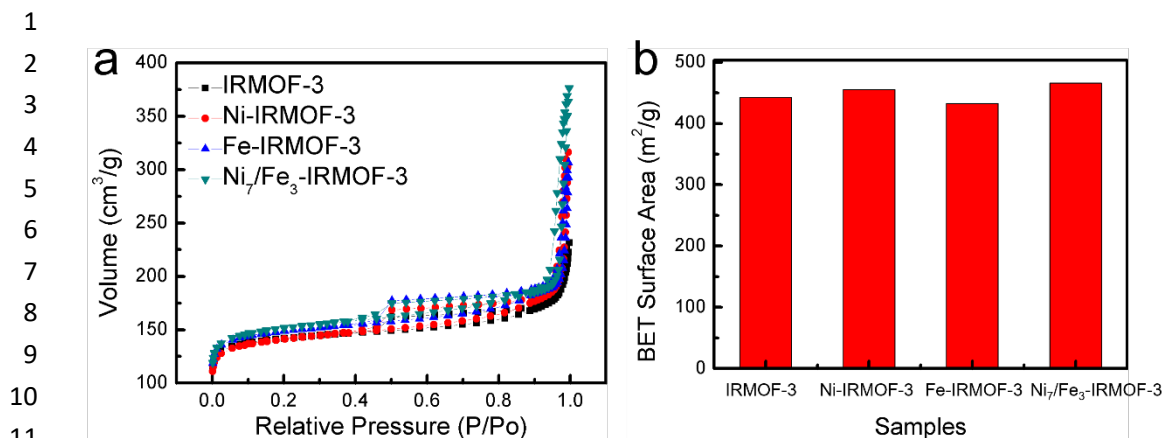


Fig. S7. (a) N_2 adsorption and desorption isotherm and (b) BET surface areas for IRMOF-3, Ni-IRMOF-3, Fe-IRMOF-3 and Ni_7/Fe_3 -IRMOF-3.

14
15
16
17
18
19
20
21
22
23
24
25
26
27
28
29
30
31
32
33
34
35
36
37
38
39
40
41
42
43
44

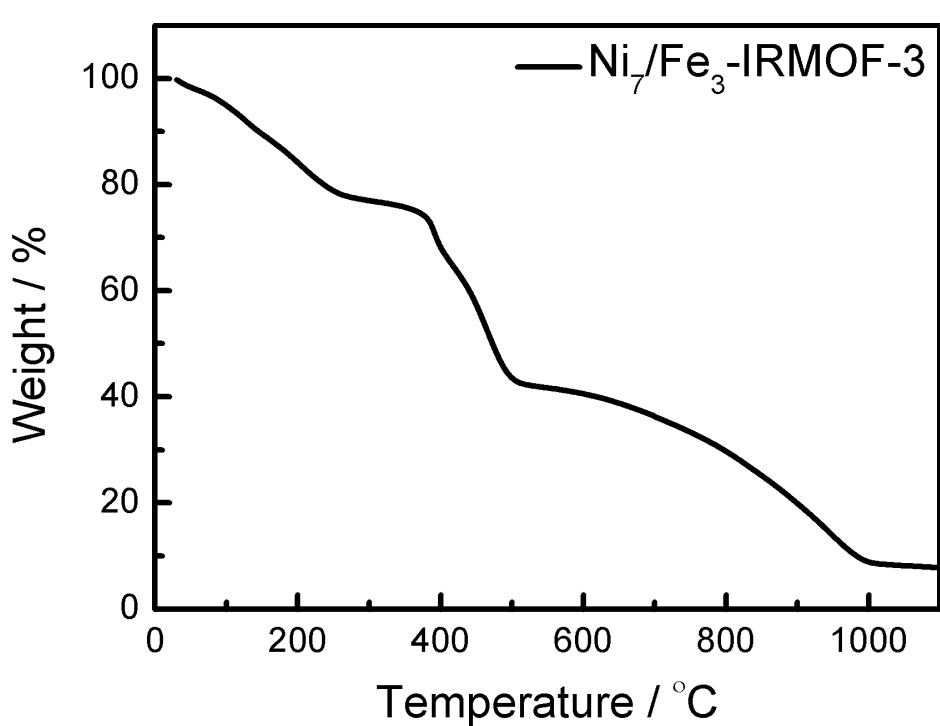


Fig. S8. TGA patterns of Ni_7/Fe_3 -IRMOF-3.

Table S1. Ni and Fe loading ratios of different samples.

Samples	Feeding mass (Ni)	Final product ratio (Ni)	Feeding mass (Fe)	Final product ratio (Fe)
Ni-N-C	2.41×10^{-3} mmol	0.38 %	/	/
Fe-N-C	/	/	2.59×10^{-3} mmol	0.7 %
Ni_7/Fe_3 -N-C	1.69×10^{-3} mmol	0.30 %	7.77×10^{-4} mmol	0.45 %

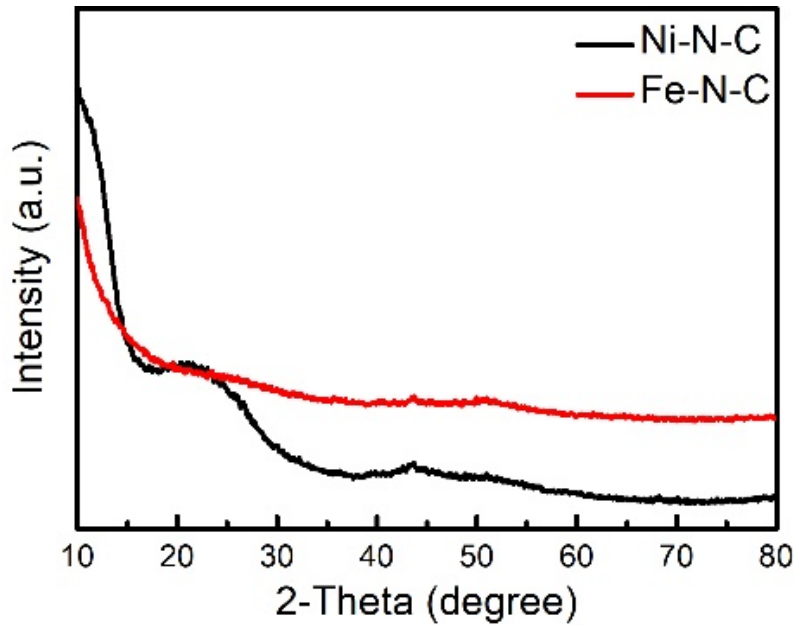


Fig. S9. XRD patterns of Ni-N-C and Fe-N-C.

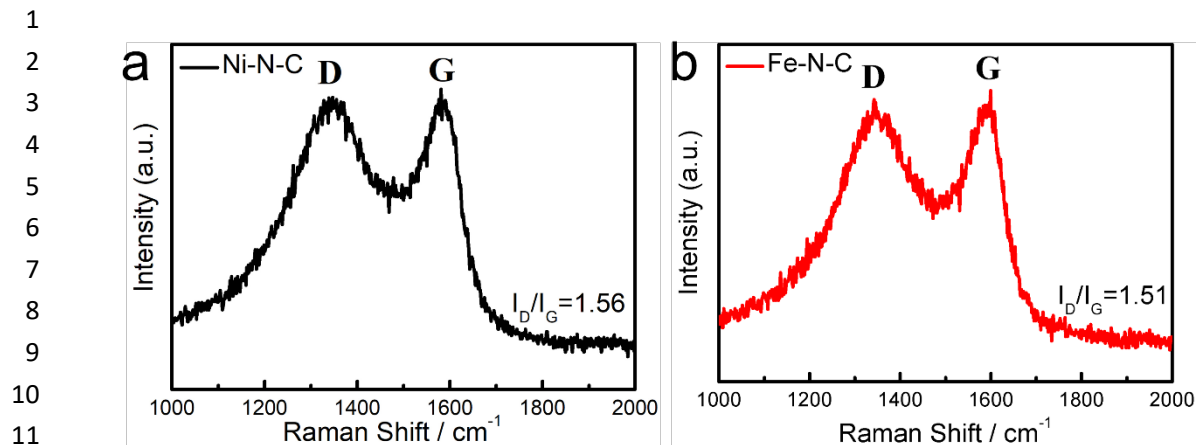


Fig. S10. Raman spectra of (a) Ni-N-C and (b) Fe-N-C.

1
2
3
4
5
6
7
8
9
10
11
12
13
14
15
16
17
18
19
20
21
22
23
24
25
26
27
28
29
30
31
32
33
34
35
36
37
38
39
40
41
42
43
44

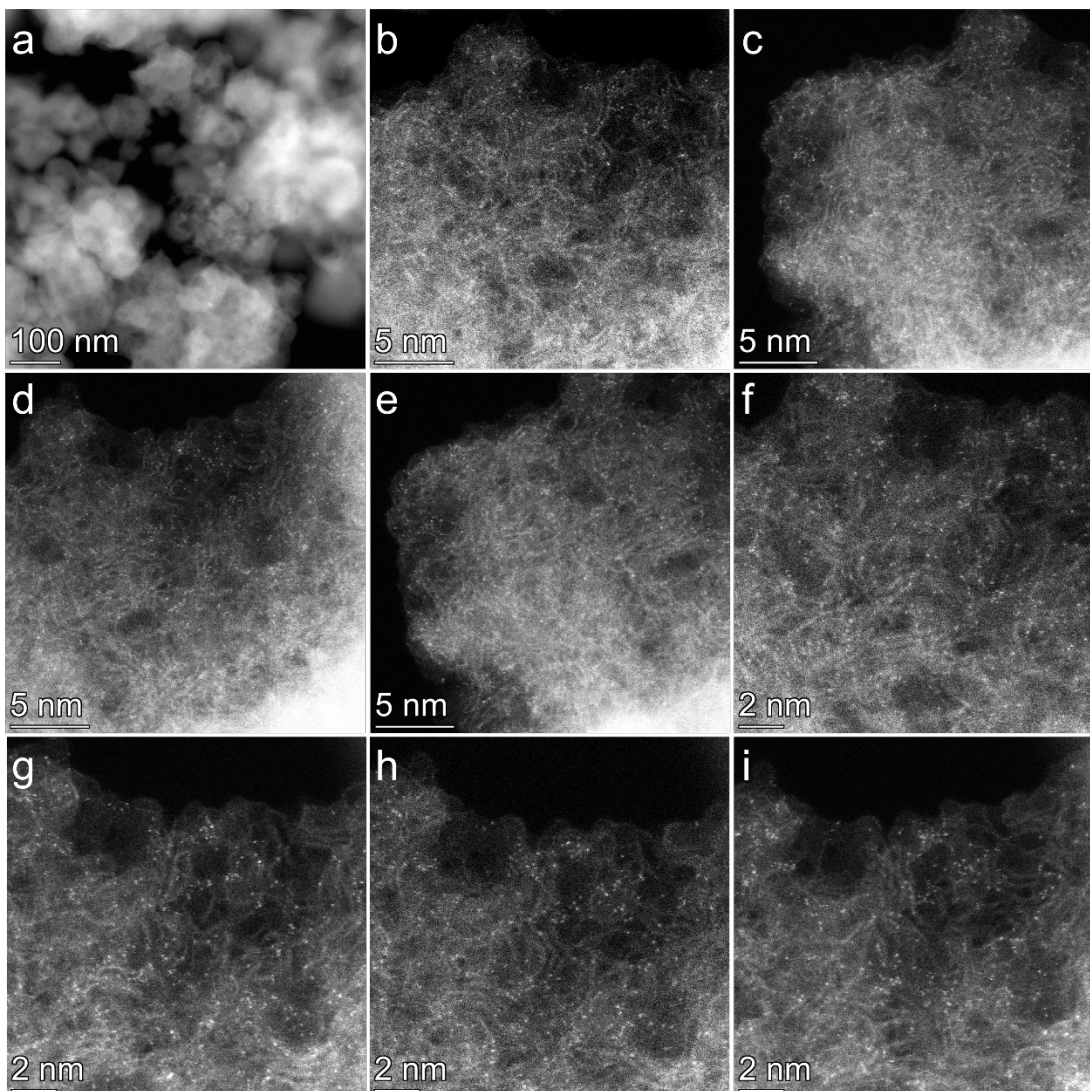
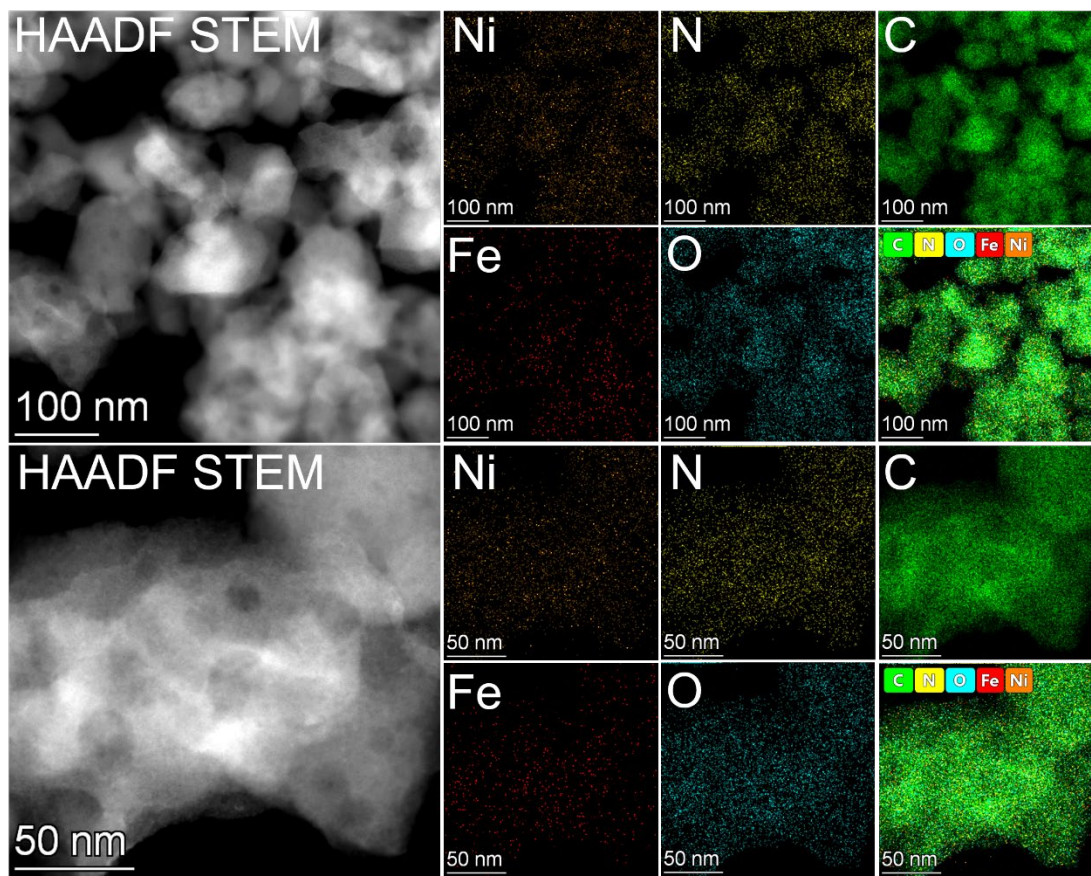


Fig. S11. (a) Low magnification and (b-i) high magnification aberration-corrected HAADF STEM images of Ni₇/Fe₃-N-C sample.



23 Fig. S12. HAADF STEM image of $\text{Ni}_7/\text{Fe}_3\text{-N-C}$ and representative EDX chemical composition
 24 maps.

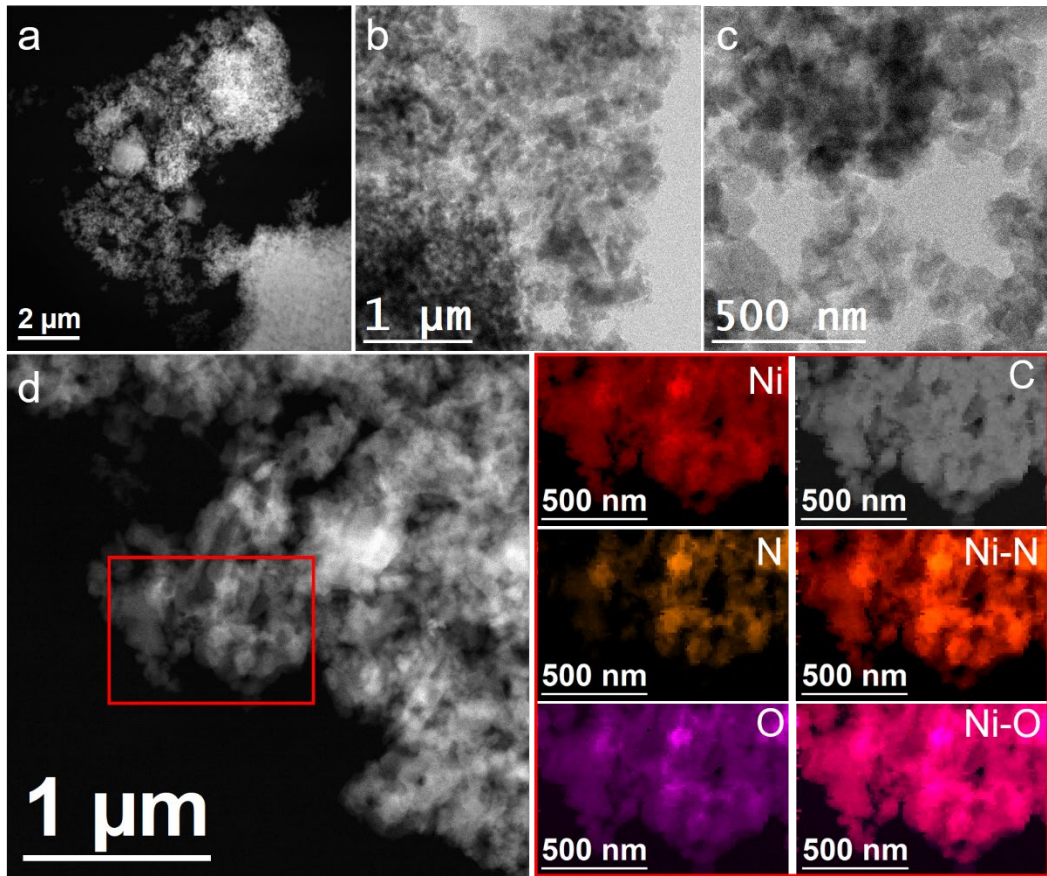


Fig. S13. (a) HAADF STEM, (b, c) BF TEM images of Ni-N-C, (d) HAADF STEM image and representative EELS chemical composition maps obtained from the red squared area of the STEM micrograph. Individual Ni L_{2,3}-edges at 855 eV (red), N K-edges at 401 eV (orange), O K-edges at 532 eV (pink) and C K-edges at 285 eV (grey) as well as composites of Ni-N and Ni-O.

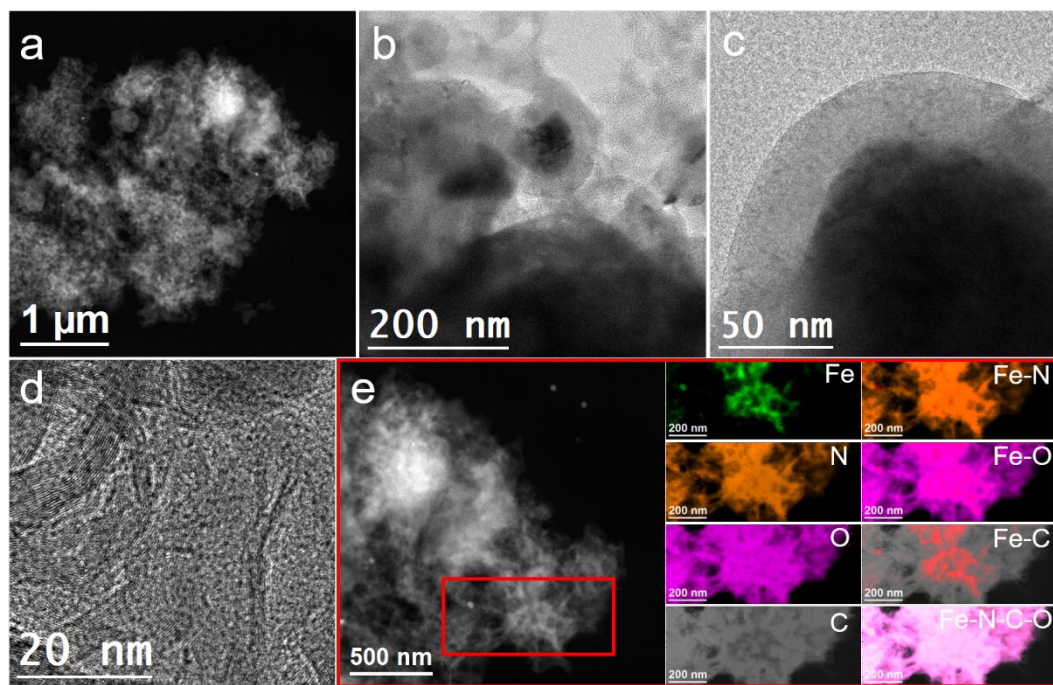


Fig. S14. (a) HAADF STEM, (b, c) BF TEM, (d) HRTEM images of Fe-N-C as well as (e) HAADF STEM image and representative EELS chemical composition maps obtained from the red squared area of the STEM micrograph. Individual Fe L_{2,3}-edges at 708 eV (green), N K-edges at 401 eV (orange), O K-edges at 532 eV (pink) and C K-edges at 285 eV (grey) as well as composites of Fe-N, Fe-O, Fe-C and Fe-N-C-O.

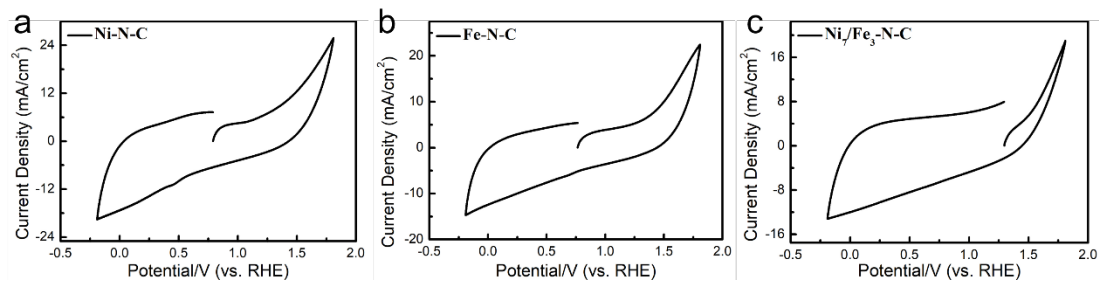


Fig. S15. CV curves of (a) Ni-N-C, (b) Fe-N-C and (c) $\text{Ni}_7/\text{Fe}_3\text{-N-C}$ in 0.5 M NaHCO_3 electrolyte.

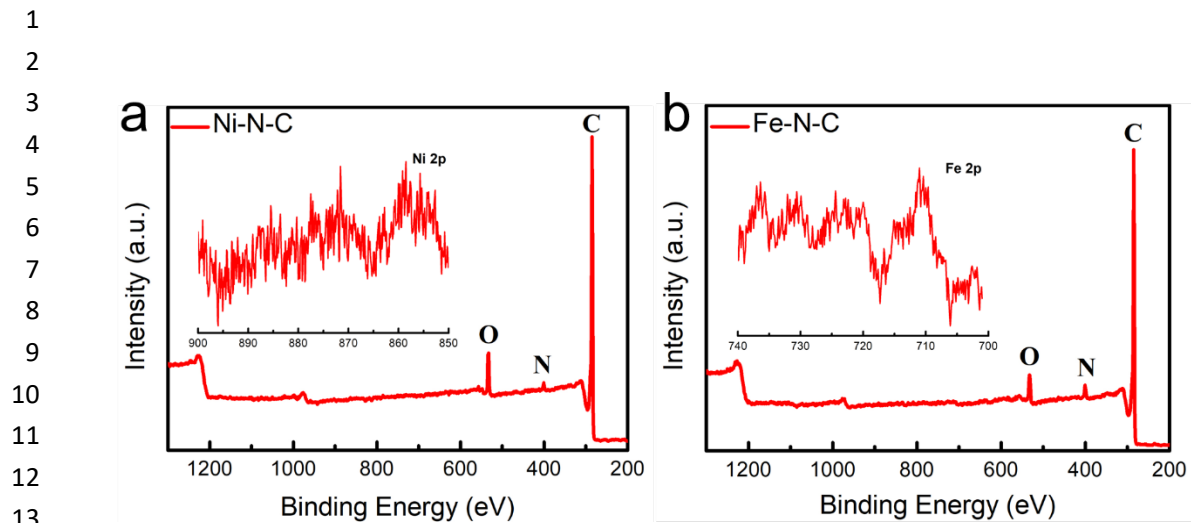


Fig. S16. XPS survey spectra of (a) Ni-N-C (inset) Ni 2p and (b) Fe-N-C (inset) Fe 2p.

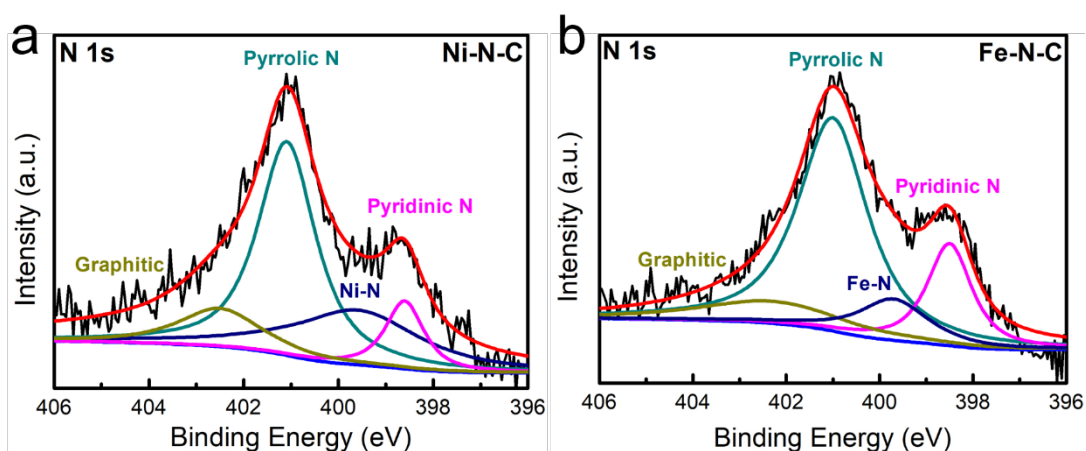


Fig. S17. High-resolution XPS N 1s of (a) Ni-N-C and (b) Fe-N-C.

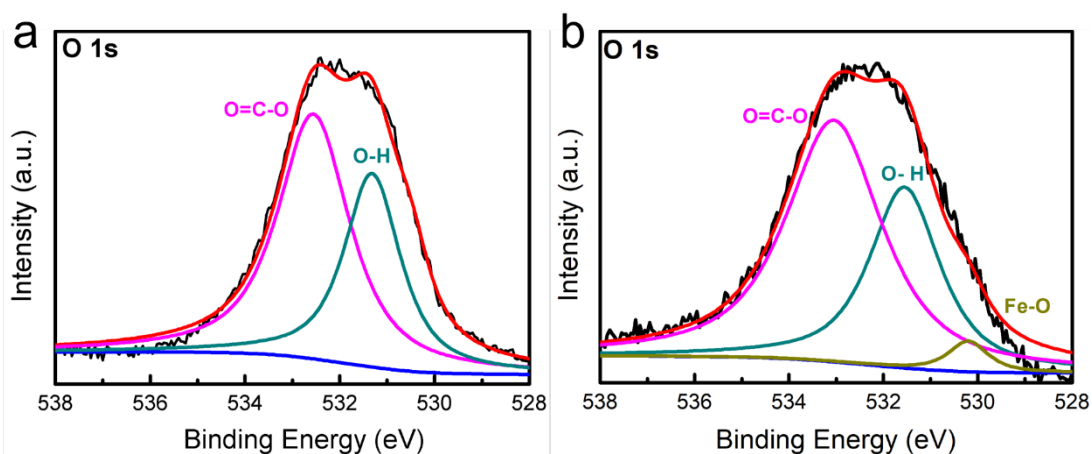


Fig. S18. High-resolution XPS O 1s of (a) Ni-N-C and (b) Fe-N-C.

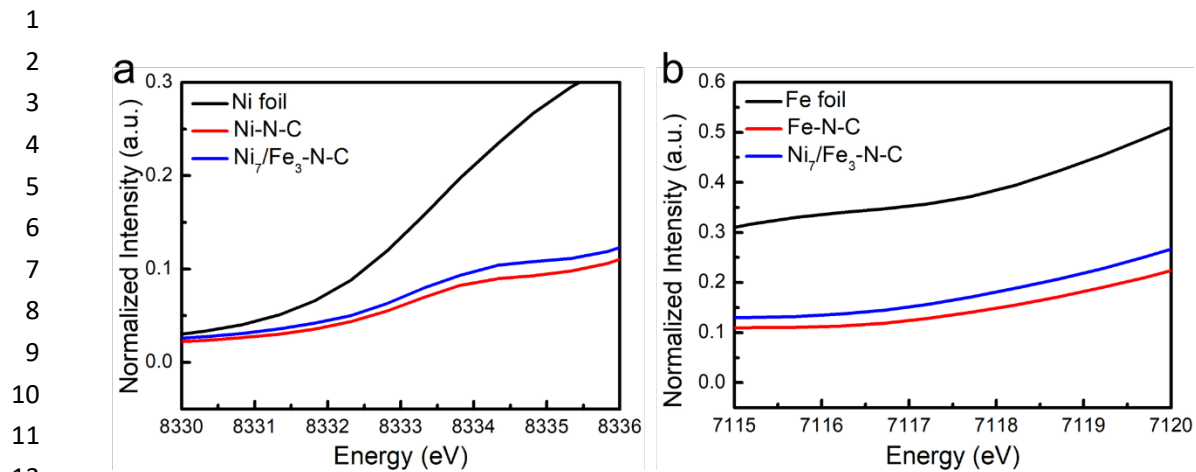


Fig. S19. The enlarged pre-edge region of (a) Ni K-edge XANES spectra and (b) Fe K-edge XANES spectra.

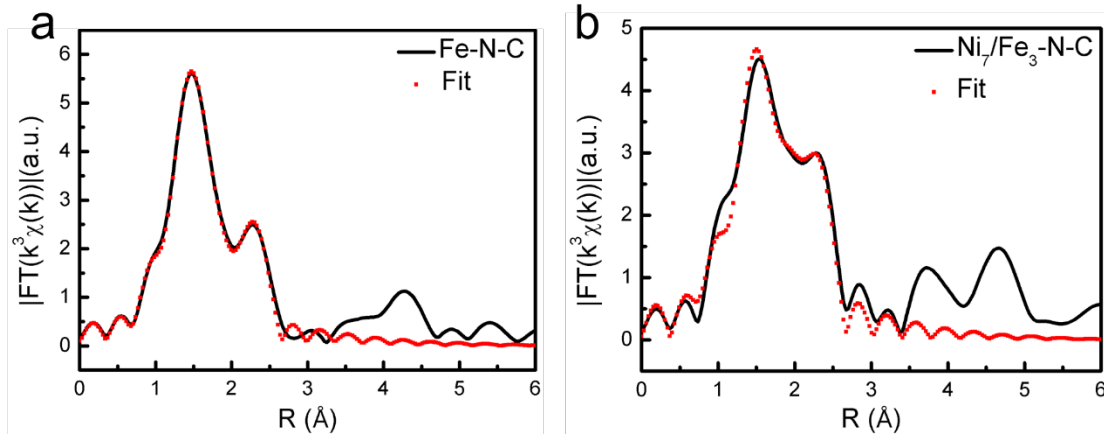


Figure S20. The corresponding Fe K-edge EXAFS fitting parameters for (a) Fe-N-C and (b) Ni₇/Fe₃-N-C samples.

Table S2. EXAFS fitting parameters at the Ni K-edge for various samples

Sample	Shell	N ^a	R (Å) ^b	σ^2 (Å ² ·10 ⁻³) ^c	ΔE_0 (eV) ^d	R factor (%)
Ni ₇ /Fe ₃ -N-C	Ni-N	4.5	1.84	9.2	-5.1	0.3
Ni-N-C	Ni -N	3.9	1.87	6.5	-5.9	0.7
	Ni -C	3.2	2.12	6.3	-1.6	

^aN: coordination numbers; ^bR: bond distance; ^c σ^2 : Debye-Waller factors; ^d ΔE_0 : the inner potential correction. R factor: goodness of fit. S02 were set as 0.85/0.80 for Ni-N/Ni-C, which was obtained from the experimental EXAFS fit of reference FePc by fixing CN as the known crystallographic value and was fixed to all the samples.

Table S3. EXAFS fitting parameters at the Fe K-edge for various samples

Sample	Shell	N ^a	R (Å) ^b	σ^2 (Å ² ·10 ⁻³) ^c	ΔE_0 (eV) ^d	R factor (%)
Ni ₇ /Fe ₃ -N-C	Fe-N(O)	4.8	1.98	8.9	-2.4	1.1
Fe-N-C	Fe-N	6.1	1.99	10.1	-3.3	0.3
	Fe-Fe	1.0	2.52	7.2	-1.5	

^aN: coordination numbers; ^bR: bond distance; ^c σ^2 : Debye-Waller factors; ^d ΔE_0 : the inner potential correction. R factor: goodness of fit. S02 were set as 0.85/0.90 for Fe-N/Fe-Fe, which was obtained from the experimental EXAFS fit of reference FePc/Fe foil by fixing CN as the known crystallographic value and was fixed to all the samples.

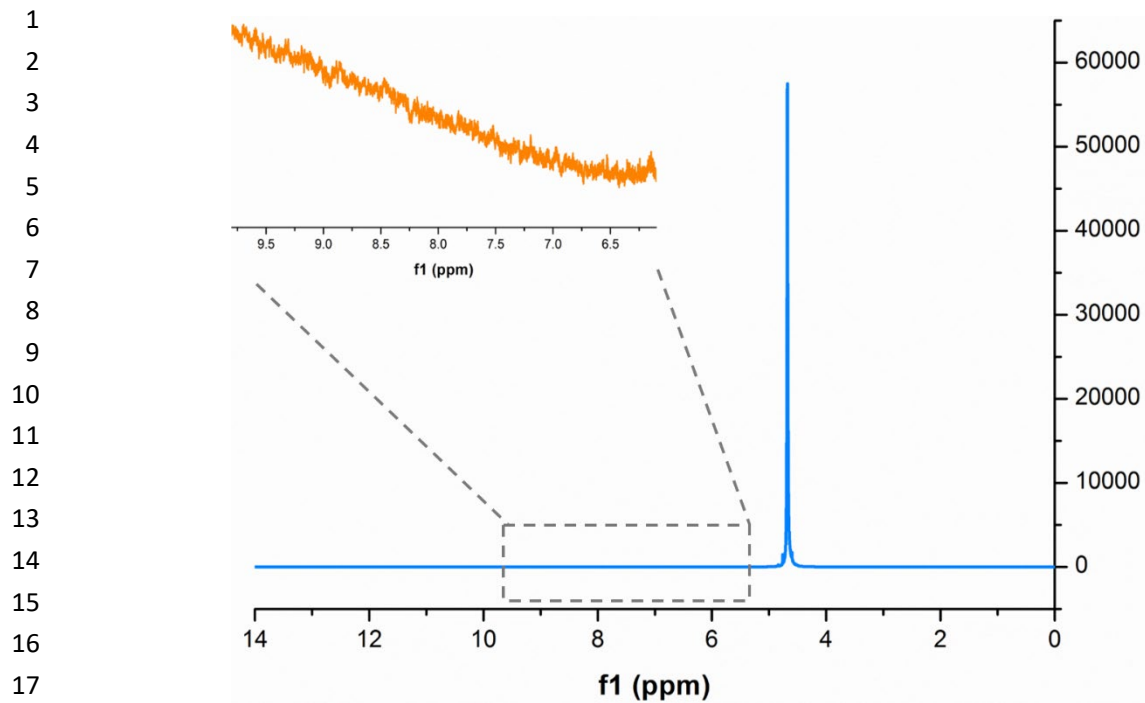


Fig. S21. The representative ¹H-NMR spectra of the electrolyte after electrolysis of -0.50 V for Ni₇/Fe₃-N-C in CO₂-saturated 0.5 M NaHCO₃ electrolyte for 30 h.

20
21
22
23
24
25
26
27
28
29
30
31
32
33
34
35
36
37
38
39
40
41
42
43
44

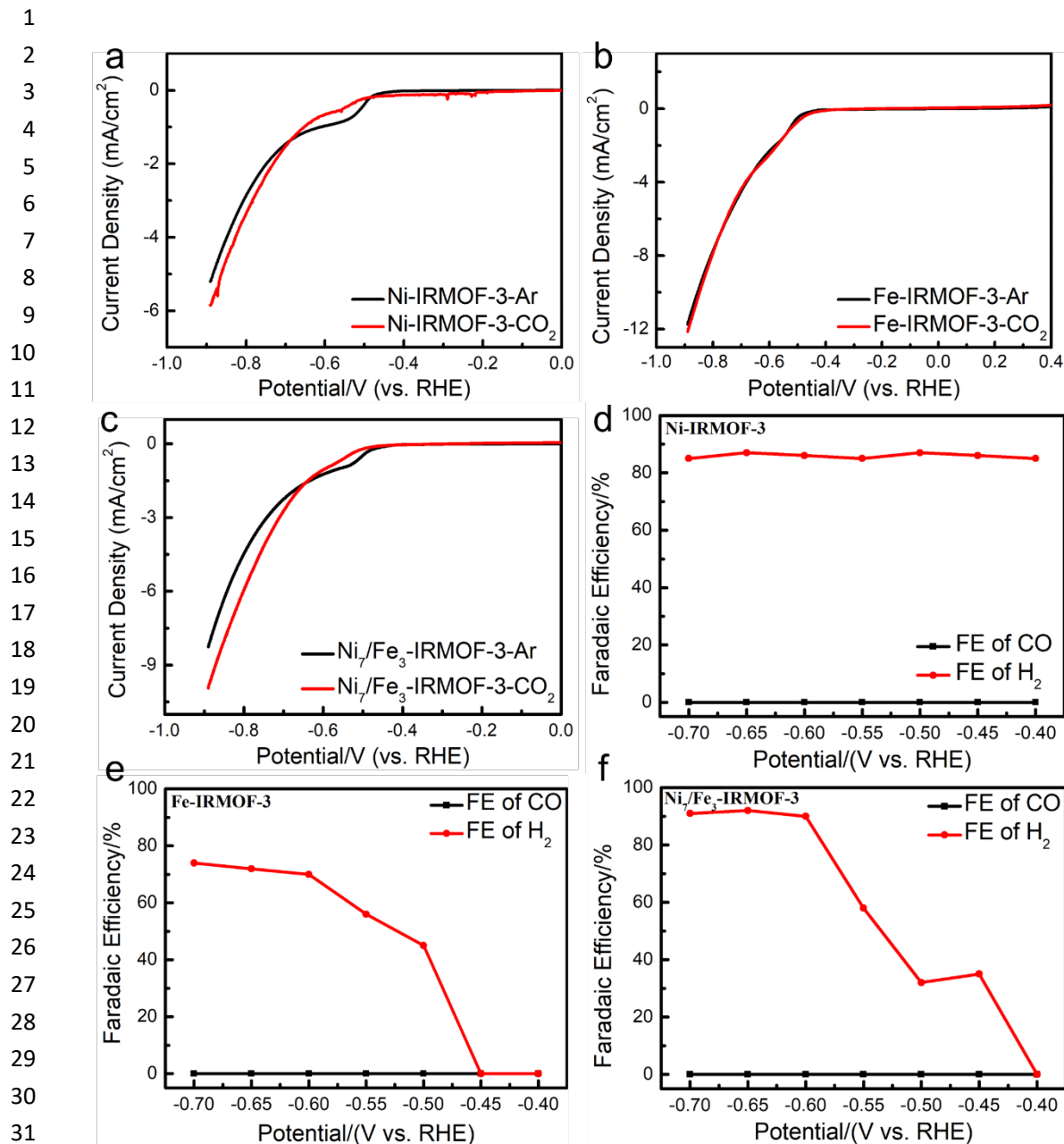


Fig. S22. LSV curves vs. RHE of (a) Ni-IRMOF-3, (b) Fe-IRMOF-3, and (c) Ni₇/Fe₃-IRMOF-3 obtained in Ar- or CO₂-saturated 0.5 M NaHCO₃ solution. FE of CO at various potentials and FE of H₂ at various potentials on (d) Ni-IRMOF-3, (e) Fe-IRMOF-3, (f) Ni₇/Fe₃-IRMOF-3.

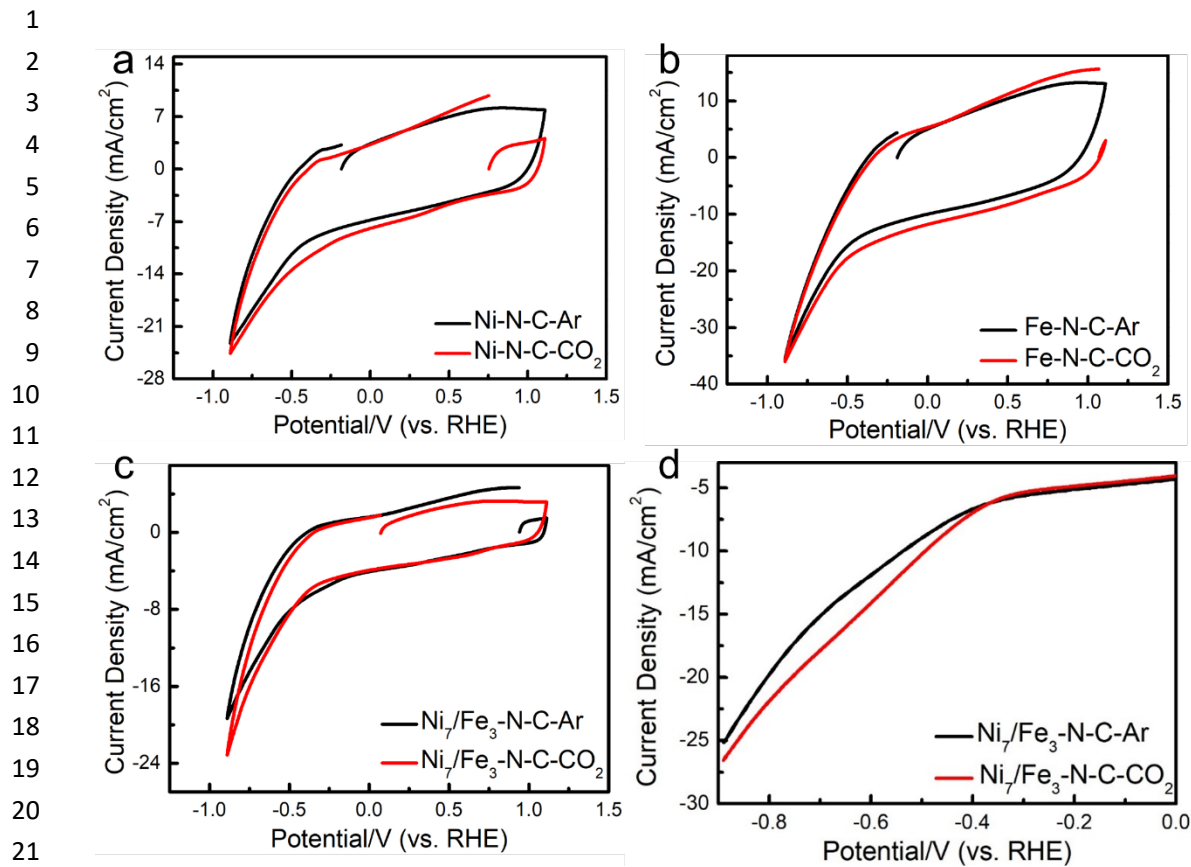
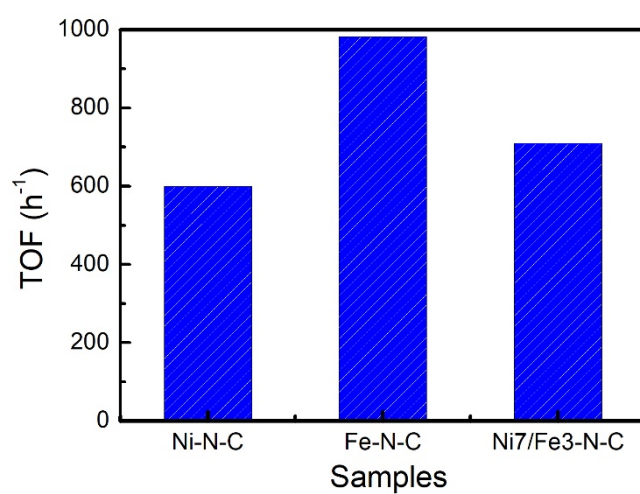


Fig. S23. CV curves vs. RHE of (a) Ni-N-C, (b) Fe-N-C, (c) Ni₇/Fe₃-N-C and (d) LSV curves vs. RHE of Ni₇/Fe₃-N-C obtained in Ar- or CO₂-saturated 0.5 M NaHCO₃ solution.



14 **Fig. S24.** TOF value of different samples.
15
16
17
18
19
20
21
22
23
24
25
26
27
28
29
30
31
32
33
34
35
36
37
38
39
40
41
42
43
44

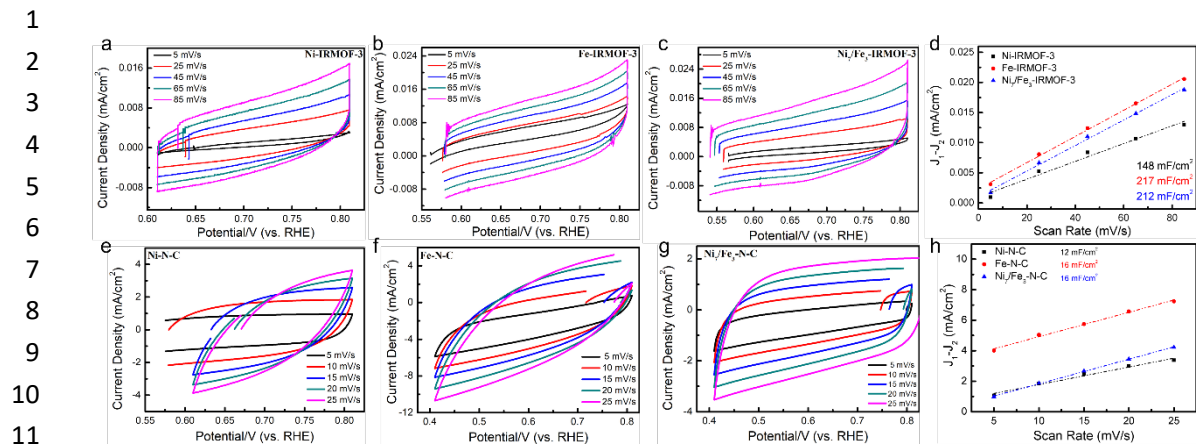


Fig. S25. Cyclic voltammograms curves for (a) Ni-IRMOF-3, (b) Fe-IRMOF-3, (c) Ni₇/Fe₃-IRMOF-3, (e) Ni-N-C, (f) Fe-N-C and (g) Ni₇/Fe₃-N-C. (d) Plots of the current density vs. scan rate for Ni-IRMOF-3, Fe-IRMOF-3 and Ni₇/Fe₃-IRMOF-3 electrodes. (h) Plots of the current density vs. scan rate for Ni-N-C, Fe-N-C and Ni₇/Fe₃-N-C electrodes.

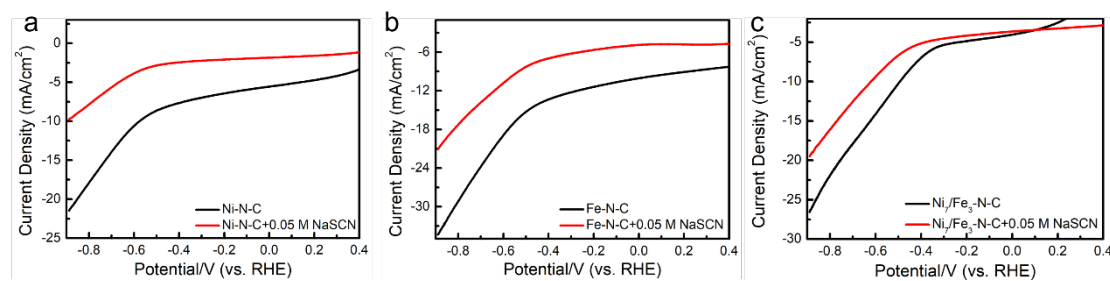


Fig. S26. Linear sweep voltammetry curves of (a) Ni-N-C, (b) Fe-N-C and (c) $\text{Ni}_7\text{Fe}_3\text{-N-C}$ with and without 0.05 M NaSCN.

1
2
3
4
5
6
7
8
9
10
11
12
13
14
15
16
17
18
19
20
21
22
23
24
25
26
27
28
29
30
31
32
33
34
35
36
37
38
39
40
41
42
43
44

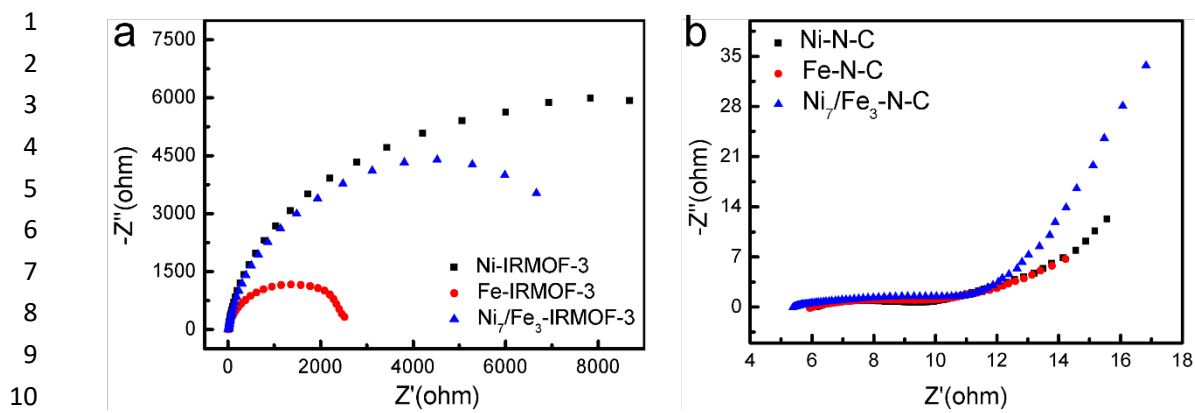


Fig. S27. Electrochemical impedance spectroscopy (EIS) of (a) Ni-IRMOF-3, Fe-IRMOF-3 and Ni_7/Fe_3 -IRMOF-3, as well as (b) Ni-N-C, Fe-N-C and Ni_7/Fe_3 -N-C.

13
14
15
16
17
18
19
20
21
22
23
24
25
26
27
28
29
30
31
32
33
34
35
36
37
38
39
40
41
42
43
44

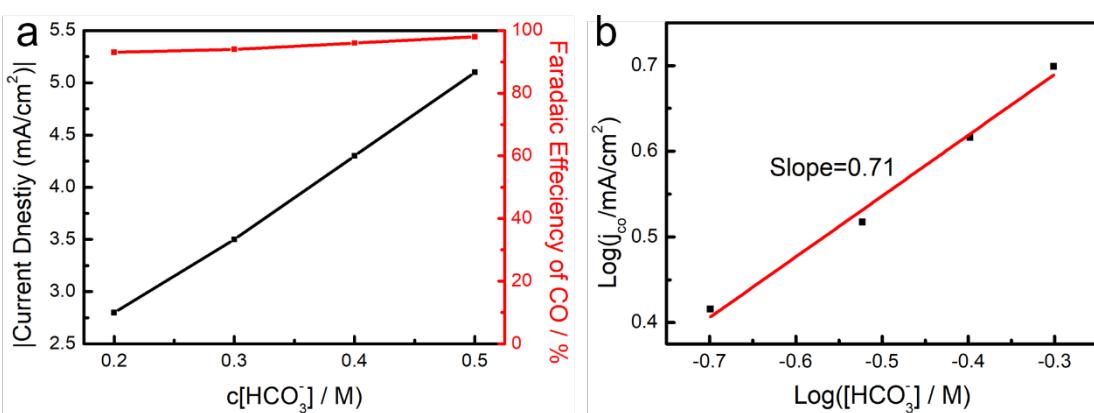


Fig. S28. (a) Current density and FE of $\text{Ni}_7/\text{Fe}_3\text{-N-C}$ at different NaHCO_3 concentration at a constant potential (-0.50 V vs. RHE). (b) Partial CO current density of $\text{Ni}_7/\text{Fe}_3\text{-N-C}$ vs. NaHCO_3 concentration at -0.50 V vs. RHE.

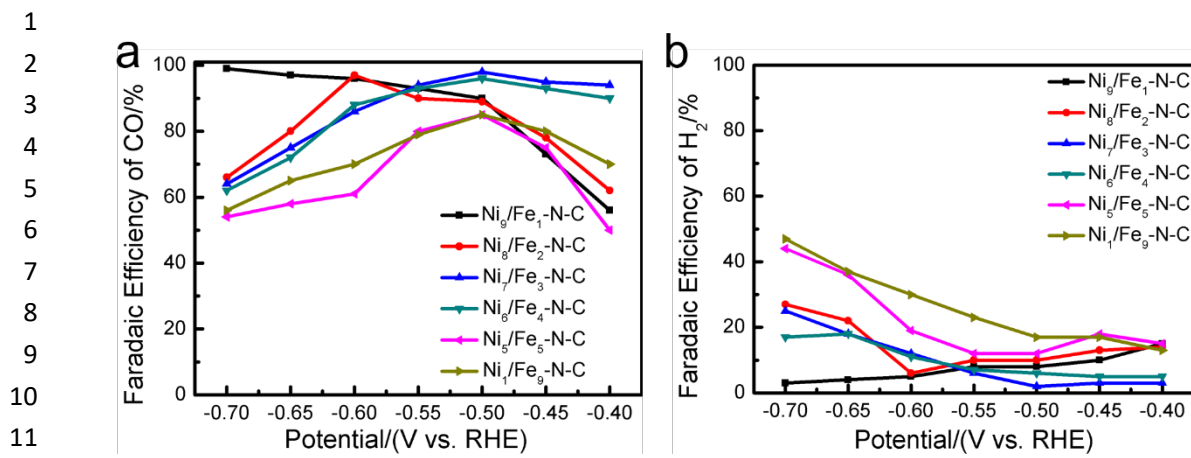


Fig. S29. (a) FE of CO and (b) FE of H₂ at various potentials on Ni_x/Fe_y-N-C.

12
13
14
15
16
17
18
19
20
21
22
23
24
25
26
27
28
29
30
31
32
33
34
35
36
37
38
39
40
41
42
43
44

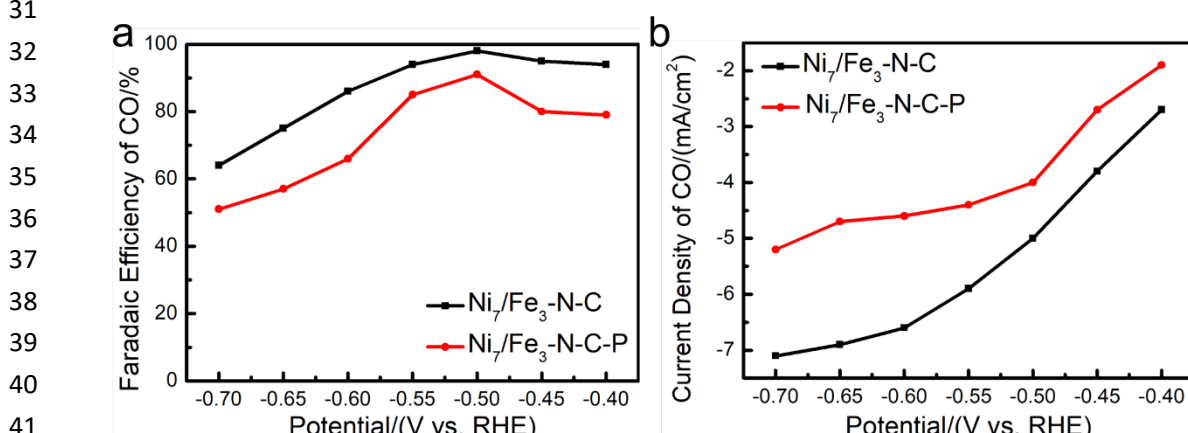
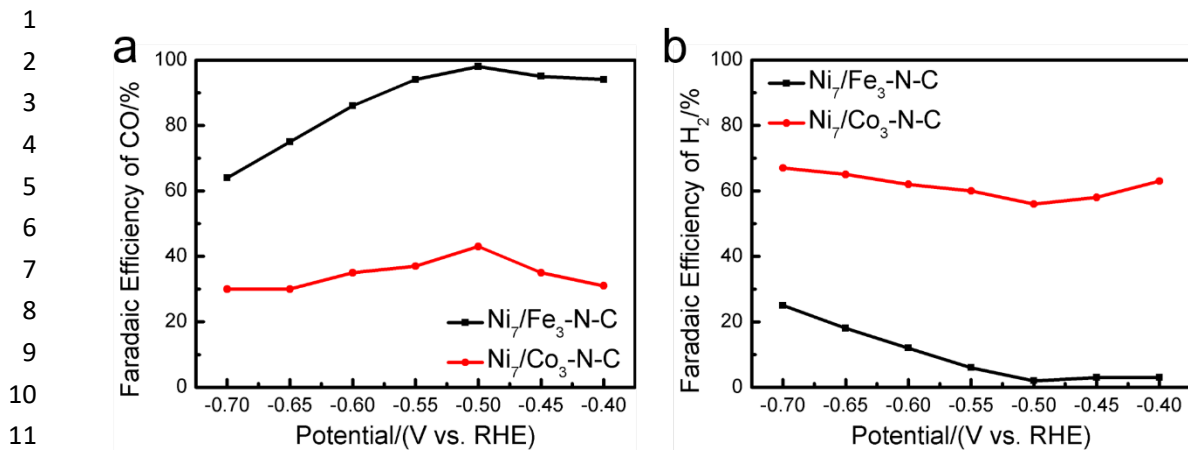


Fig. S31. (a) FE of CO at various potentials and (b) Current density for CO production on Ni₇/Fe₃-N-C and Ni₇/Fe₃-N-C-P.

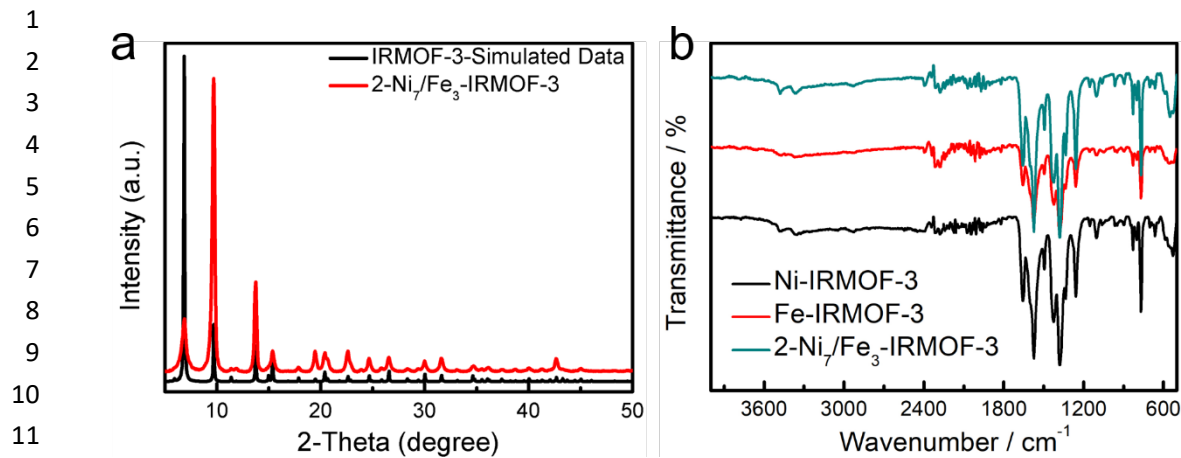


Fig. S32. (a) XRD patterns and (b) FTIR image of 2-Ni₇/Fe₃-IRMOF-3.

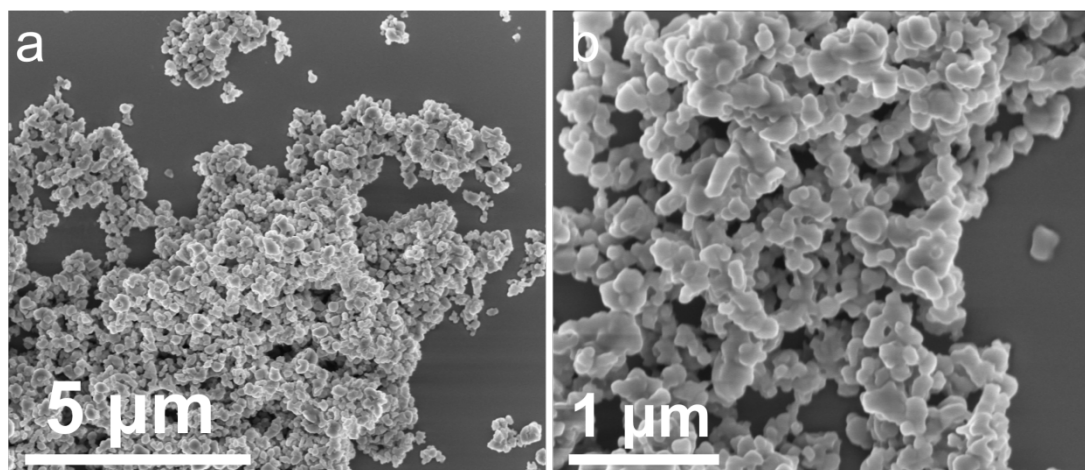


Fig. S33. SEM images of 2-Ni₇/Fe₃-IRMOF-3.

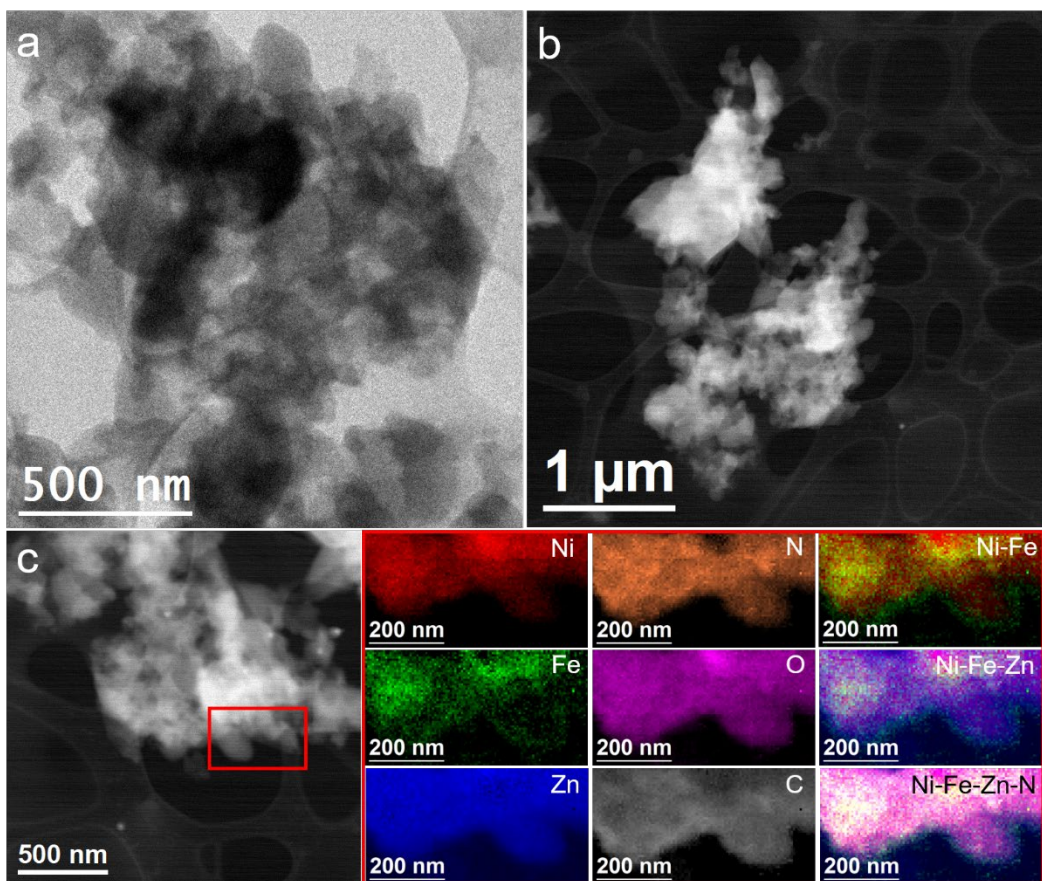


Fig. S34. (a) BF TEM, (b and c) HAADF STEM image of 2-Ni₇/Fe₃-IRMOF-3 and representative EELS chemical composition maps obtained from the red squared area of the STEM micrograph. Individual Ni L_{2,3}-edges at 855 eV (red), Fe L_{2,3}-edges at 708 eV (green), Zn L_{2,3}-edges at 1020 eV (blue), N K-edges at 401 eV (orange), O K-edges at 532 eV (pink) and C K-edges at 285 eV (grey) as well as composites of Ni-Fe, Ni-Fe-Zn and Ni-Fe-Zn-N.

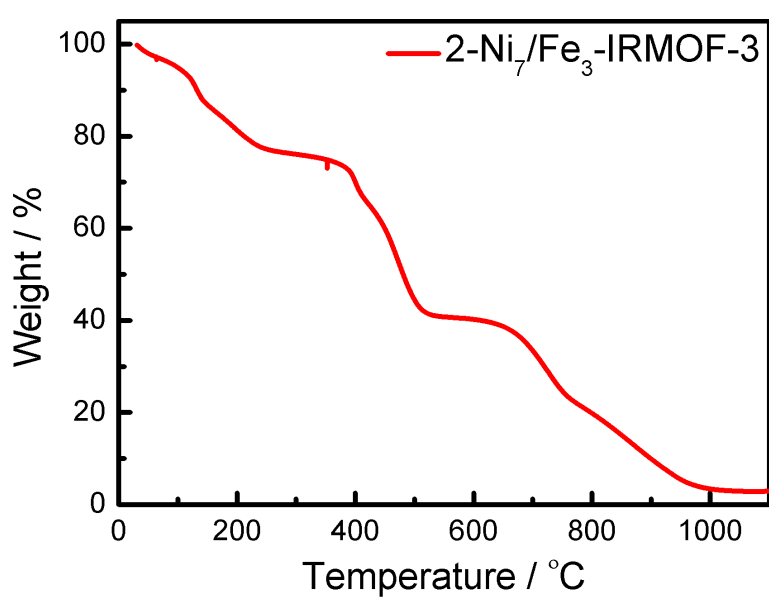


Fig. 35. TGA of 2-Ni₇/Fe₃-IRMOF-3.

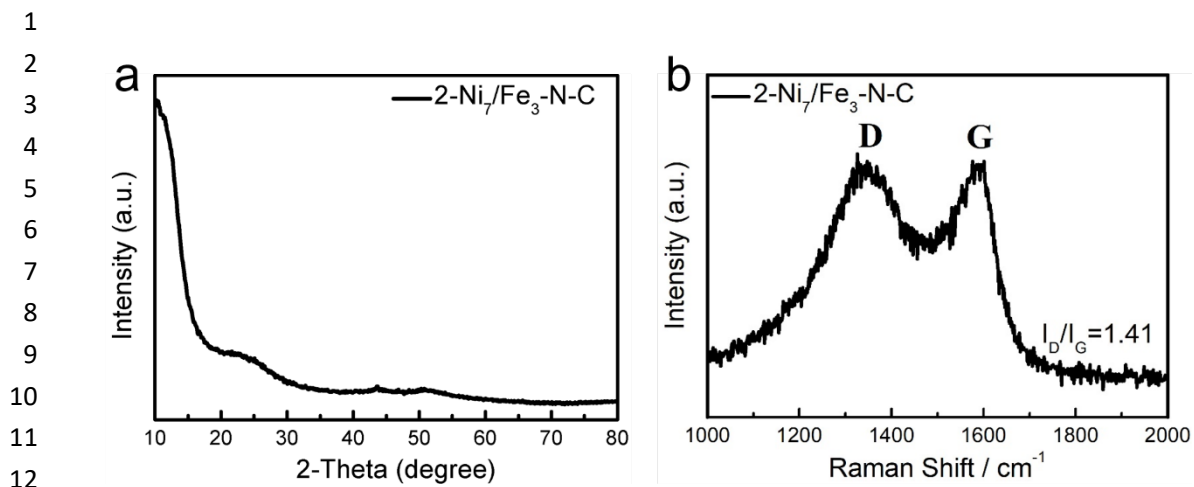


Fig. S36. (a) XRD patterns and (b) Raman spectra of 2-Ni₇/Fe₃-N-C.

1
2
3
4
5
6
7
8
9
10
11
12
13
14
15
16
17
18
19
20
21
22
23
24
25
26
27
28
29
30
31
32
33
34
35
36
37
38
39
40
41
42
43
44

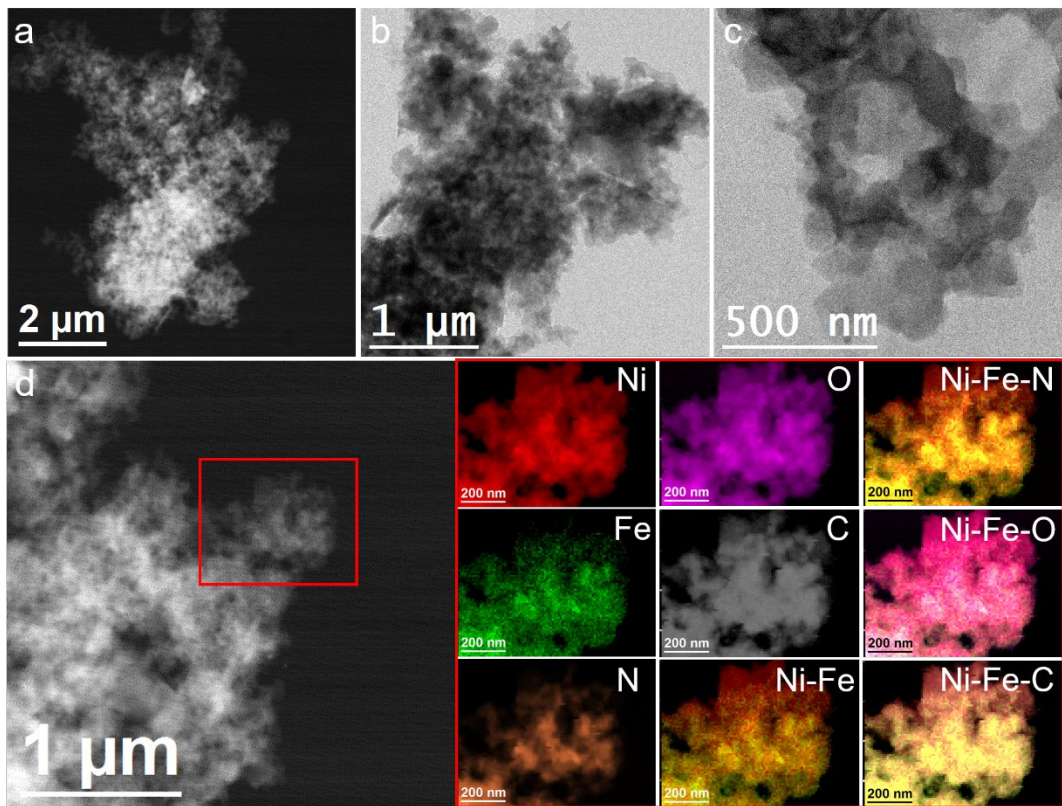


Fig. S37. (a) HAADF STEM, (b, c) BF TEM images of 2-Ni₇/Fe₃-N-C, (d) HAADF STEM image and representative EELS chemical composition maps obtained from the red squared area of the STEM micrograph. Individual Ni L_{2,3}-edges at 855 eV (red), Fe L_{2,3}-edges at 708 eV (green), N K-edges at 401 eV (orange), O K-edges at 532 eV (pink) and C K-edges at 285 eV (grey) as well as composites of Ni-Fe, Ni-Fe-N, Ni-Fe-O and Ni-Fe-C.

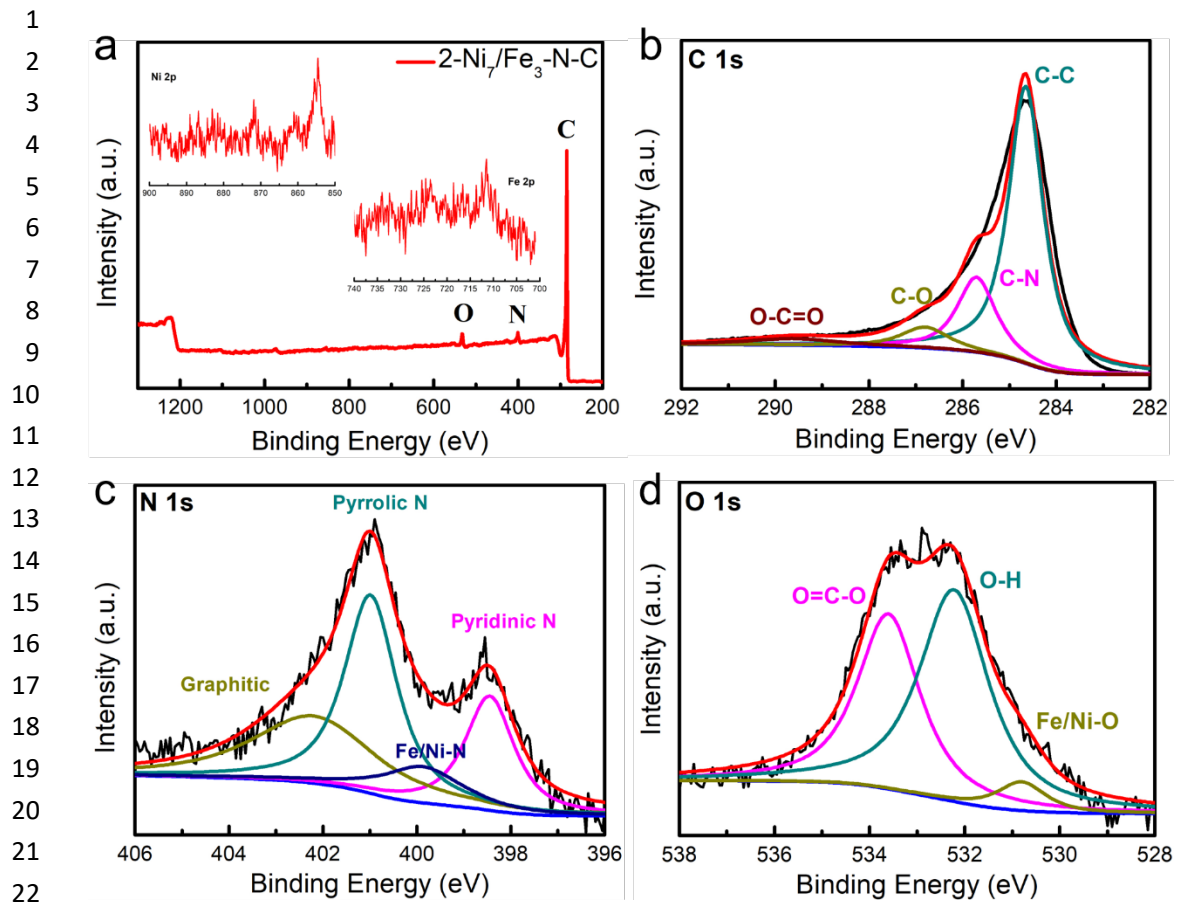


Fig. S38. XPS spectra for the (a) survey scan, (inset) Ni 2p and Fe 2p, (b) C 1s, (c) N 1s and (d) O 1s of 2-Ni₇/Fe₃-N-C.

25
26
27
28
29
30
31
32
33
34
35
36
37
38
39
40
41
42
43
44

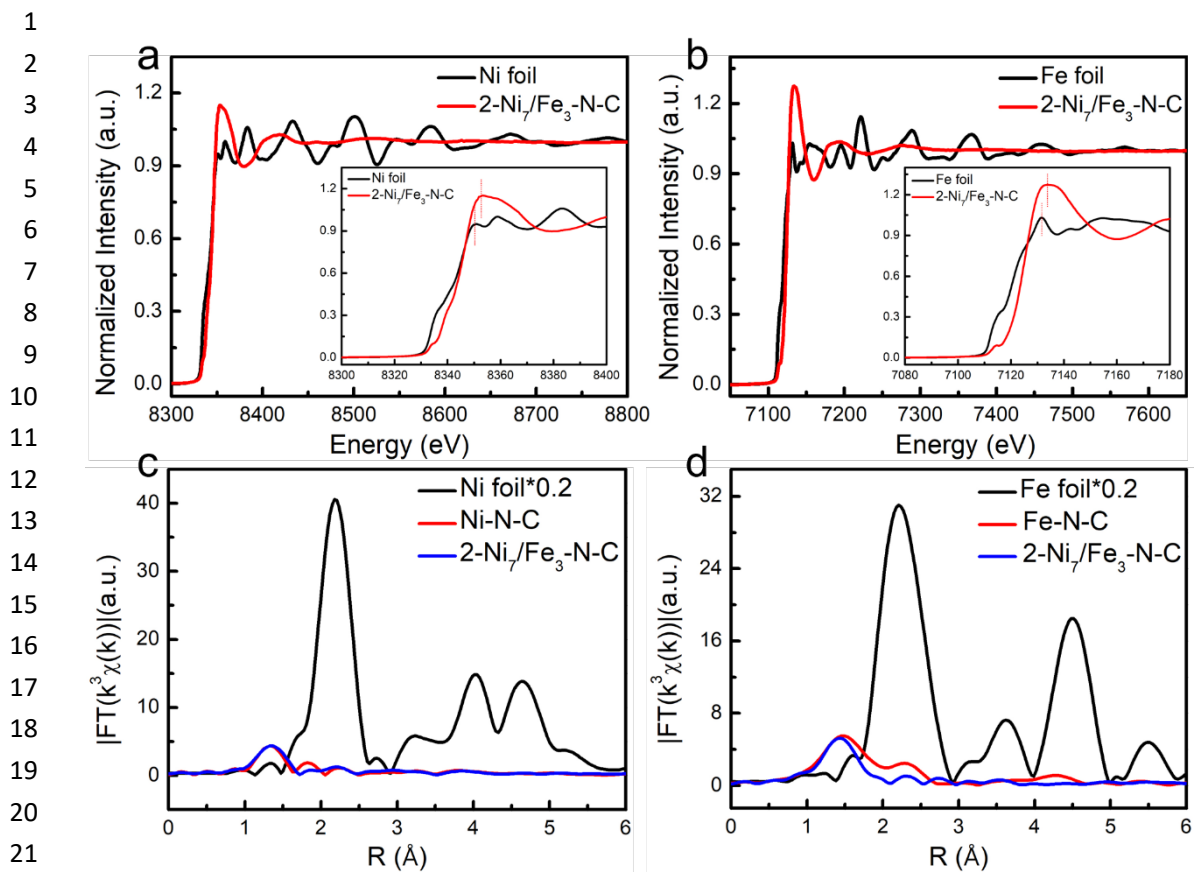


Fig. S39. (a) Ni K-edge XANES spectra of Ni foil and 2-Ni₇/Fe₃-N-C. (b) Fe K-edge XANES spectra of Fe foil and 2-Ni₇/Fe₃-N-C. (c and d) Fourier transformation of the EXAFS spectra at R space.

25
26
27
28
29
30
31
32
33
34
35
36
37
38
39
40
41
42
43
44

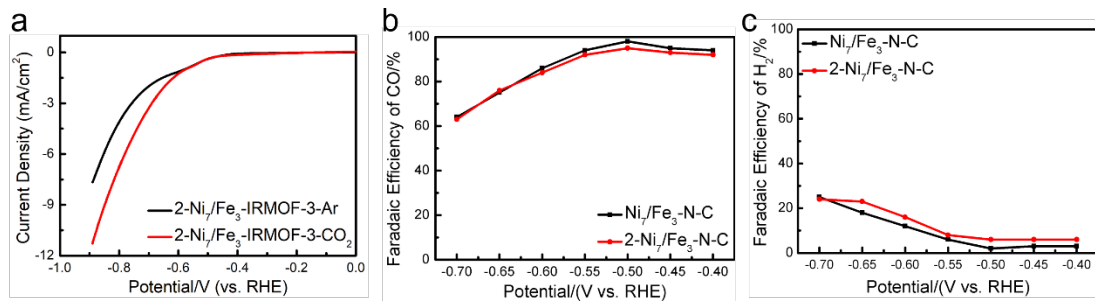


Fig. S40. (a) LSV of 2-Ni₇/Fe₃-N-C obtained in Ar- or CO₂-saturated 0.5 M NaHCO₃ solution. FE of (b) CO and (c) FE of H₂ at various potentials on Ni₇/Fe₃-N-C and 2-Ni₇/Fe₃-N-C.

1
2
3
4
5
6
7
8
9
10
11
12
13
14
15
16
17
18
19
20
21
22
23
24
25
26
27
28
29
30
31
32
33
34
35
36
37
38
39
40
41
42
43
44

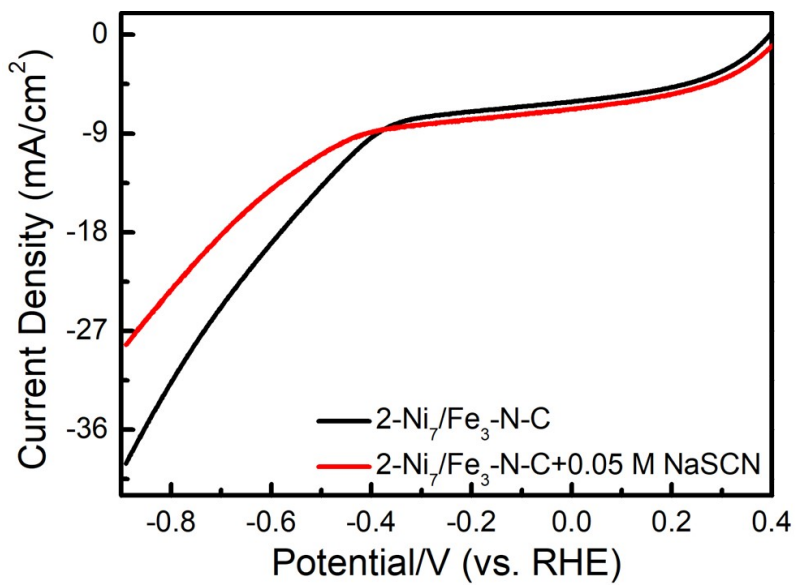
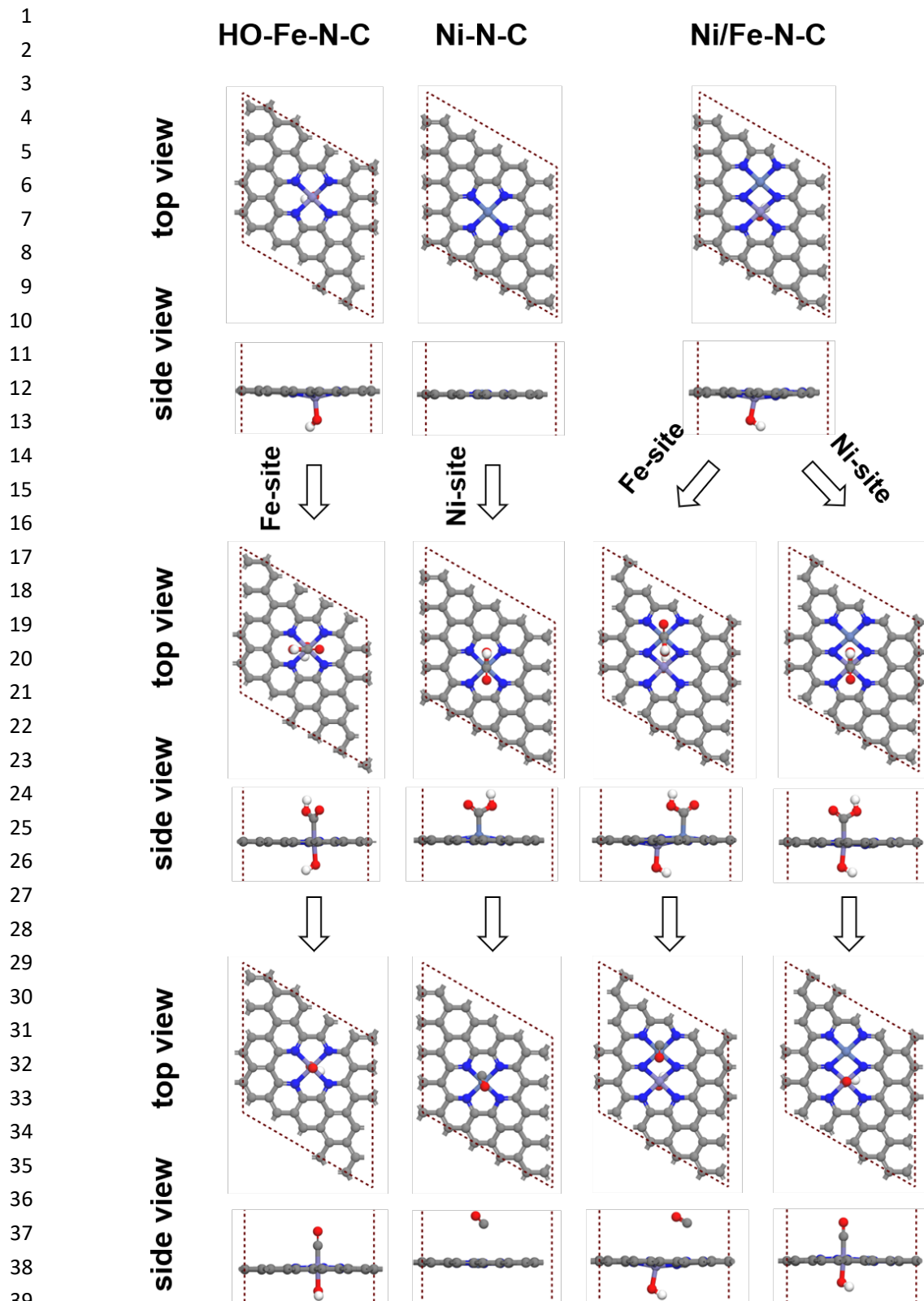


Fig. S41. Linear sweep voltammetry curves of $2\text{-Ni}_7/\text{Fe}_3\text{-N-C}$ with and without 0.05 M NaSCN.



40 **Fig. S42.** The top view and side view of optimized adsorption configuration on simulated models
 41 (Ni, Fe, O, N and C atoms are represented in purple, cyan, red, blue and grey, respectively).

1 **Table S4.** Faradaic Efficiency (CO) of the reported single/double atom-based electrocatalysts for
 2 CO₂ electroreduction.

Catalyst	Product	FE(CO)	Potential	Reference
Fe-N-C	CO	93 %	-0.60 V vs. RHE	18
Fe-N-C	CO	81 %	-0.57 V vs. RHE	19
Fe-N-C	CO	93.5 %	-0.50 V vs. RHE	20
Fe-N-C	CO	93 %	-0.60 V vs. RHE	21
Fe-N-C	CO	80 %	-0.60 V vs. RHE	22
Fe-N-C	CO	92 %	-0.58 V vs. RHE	23
Fe-N-C	CO	64 %	-0.60 V vs. RHE	24
Fe-N-C	CO	95.47 %	-0.60 V vs. RHE	25
Fe-N ₅ -C	CO	97 %	-0.46 V vs. RHE	26
Fe-N-C	CO	95 %	-0.45 V vs. RHE	27
Ni-N-C	CO	99 %	-0.68 V vs. RHE	5
Ni-N-C	CO	71.9 %	-0.90 V vs. RHE	6
Ni-N-C	CO	95 %	-0.70 V vs. RHE	28
Ni-N-C	CO	99 %	-0.81 V vs. RHE	29
Ni-N-C	CO	96 %	-0.67 V vs. RHE	30
Ni-N-C	CO	96 %	-0.86 V vs. RHE	31
Ni-N-C	CO	95 %	-0.77 V vs. RHE	32
Ni-N-C	CO	91.2 %	-0.90 V vs. RHE	33
Ni-N-C	CO	97 %	-0.70 V vs. RHE	34
Ni-N-C	CO	95 %	-0.77 V vs. RHE	35
Ni-N-C	CO	99 %	-0.80 V vs. RHE	36
Ni-N-C	CO	94 %	-0.80 V vs. RHE	37
NiCo-N-C	CO	53 %	-0.60 V vs. RHE	38
Ni/Fe-N-C	CO	98 %	-0.70 V vs. RHE	39
Ni/Fe-N-C	CO	90 %	-0.65 V vs. RHE	40
Ni/Mn-C ₃ N ₄ -CNT	CO	90 %	-0.70 V vs. RHE	41
ZnCo-N-C	CO	93.2 %	-0.50 V vs. RHE	42
Ni-N-Co	CO	96.4 %	-0.48 V vs. RHE	43
Ni₇/Fe₃-N-C	CO	98 %	-0.50 V vs. RHE	This work

3
 4
 5
 6
 7
 8
 9
 10
 11
 12
 13
 14

1 **References**

- 2 1. B. Ravel and M. Newville, *J. Synchrotron Rad.*, 2005, **12**, 537-541.
3 2. H. Baumgartel, *Nachrichten aus Chemie, Technik und Laboratorium*, 1988, **36**, 650-650.
4 3. J. J. Rehr and R. C. Albers, *Rev. Modern Phys.*, 2000, **72**, 621-654.
5 4. T. Zhang, J. Du, P. Xi and C. Xu, *ACS Appl. Mater. Interfaces*, 2017, **9**, 362-370.
6 5. T. Zheng, K. Jiang, N. Ta, Y. Hu, J. Zeng, J. Liu and H. Wang, *Joule*, 2019, **3**, 265-278.
7 6. C. Zhao, X. Dai, T. Yao, W. Chen, X. Wang, J. Wang, J. Yang, S. Wei, Y. Wu and Y. Li, *J. Am. Chem. Soc.*, 2017, **139**, 8078-8081.
8 7. J. Pei, T. Wang, R. Sui, X. Zhang, D. Zhou, F. Qin, X. Zhao, Q. Liu, W. Yan, J. Dong, L. Zheng, A. Li, J. Mao, W. Zhu, W. Chen and Z. Zhuang, *Energy Environ. Sci.*, 2021, **14**, 3019-3028.
9 8. P. E. Blöchl, *Phys. Rev. B*, 1994, **50**, 17953-17979.
10 9. G. Kresse and J. Furthmüller, *Phys. Rev. B*, 1996, **54**, 11169-11186.
11 10. G. Kresse and J. Furthmüller, *Comput. Mater. Sci.*, 1996, **6**, 15-50.
12 11. G. Kresse and D. Joubert, *Phys. Rev. B*, 1999, **59**, 1758-1775.
13 12. J. Hafner, *J. Comput. Chem.*, 2008, **29**, 2044.
14 13. J. Wellendorff, K. T. Lundgaard, A. Møgelhøj, V. Petzold, D. D. Landis, J. K. Nørskov, T. Bligaard and K. W. Jacobsen, *Phys. Rev. B*, 2012, **85**, 235149.
15 14. F. Studt, M. Behrens, E. L. Kunkes, N. Thomas, S. Zander, A. Tarasov, J. Schumann, E. Frei, J. B. Varley, F. Abild-Pedersen, J. K. Nørskov and R. Schlögl, *ChemCatChem*, 2015, **7**, 1105-1111.
16 15. F. Studt, F. Abild-Pedersen, J. B. Varley and J. K. Nørskov, *Catal. Lett.*, 2013, **143**, 71-73.
17 16. R. Christensen, H. A. Hansen and T. Vegge, *Catal. Sci. Technol.*, 2015, **5**, 4946-4949.
18 17. A. A. Peterson, F. Abild-Pedersen, F. Studt, J. Rossmeisl and J. K. Nørskov, *Energy Environ. Sci.*, 2010, **3**, 1311-1315.
19 18. F. Pan, H. Zhang, K. Liu, D. Cullen, K. More, M. Wang, Z. Feng, G. Wang, G. Wu and Y. Li, *ACS Catal.*, 2018, **8**, 3116-3122.
20 19. X.-M. Hu, H. H. Hval, E. T. Bjerglund, K. J. Dalgaard, M. R. Madsen, M.-M. Pohl, E. Welter, P. Lamagni, K. B. Buhl, M. Bremholm, M. Beller, S. U. Pedersen, T. Skrydstrup and K. Daasbjerg, *ACS Catal.*, 2018, **8**, 6255-6264.
21 20. X. Qin, S. Zhu, F. Xiao, L. Zhang and M. Shao, *ACS Energy Letters*, 2019, **4**, 1778-1783.
22 21. X. Li, S. Xi, L. Sun, S. Dou, Z. Huang, T. Su and X. Wang, *Adv. Sci.*, 2020, **7**, 2001545.
23 22. C. Zhang, S. Yang, J. Wu, M. Liu, S. Yazdi, M. Ren, J. Sha, J. Zhong, K. Nie, A. S. Jalilov, Z. Li, H. Li, B. I. Yakobson, Q. Wu, E. Ringe, H. Xu, P. M. Ajayan and J. M. Tour, *Adv. Energy Mater.*, 2018, **8**, 1703487.
24 23. Q. Zhang, H. Jiang, D. Niu, X. Zhang, S. Sun and S. Hu, *ChemistrySelect*, 2019, **4**, 4398-4406.
25 24. J. Zhao, J. Deng, J. Han, S. Imhanria, K. Chen and W. Wang, *Chem. Engineering J.*, 2020, **389**, 124323.
26 25. J. Tuo, Y. Lin, Y. Zhu, H. Jiang, Y. Li, L. Cheng, R. Pang, J. Shen, L. Song and C. Li, *Appl. Catal. B: Environ.*, 2020, **272**, 118960.
27 26. H. Zhang, J. Li, S. Xi, Y. Du, X. Hai, J. Wang, H. Xu, G. Wu, J. Zhang, J. Lu and J. Wang, *Angew. Chem. Int. Ed.*, 2019, **58**, 14871-14876.
28 27. J. Gu, C.-S. Hsu, L. Bai, H. M. Chen and X. Hu, *Science*, 2019, **364**, 1091-1094.

- 1 28. W. Xiong, H. Li, H. Wang, J. Yi, H. You, S. Zhang, Y. Hou, M. Cao, T. Zhang and R. Cao,
2 *Small*, 2020, **16**, 2003943.
- 3 29. X. Li, W. Bi, M. Chen, Y. Sun, H. Ju, W. Yan, J. Zhu, X. Wu, W. Chu, C. Wu and Y. Xie, *J.
4 Am. Chem. Soc.*, 2017, **139**, 14889-14892.
- 5 30. S. Yang, J. Zhang, L. Peng, M. Asgari, D. Stoian, I. Kochetygov, W. Luo, E. Oveisi, O.
6 Trukhina, A. H. Clark, D. T. Sun and W. L. Queen, *Chem. Sci.*, 2020, **11**, 10991-10997.
- 7 31. Y. Lu, H. Wang, P. Yu, Y. Yuan, R. Shahbazian-Yassar, Y. Sheng, S. Wu, W. Tu, G. Liu, M.
8 Kraft and R. Xu, *Nano Energy*, 2020, **77**, 105158.
- 9 32. S.-G. Han, D.-D. Ma, S.-H. Zhou, K. Zhang, W.-B. Wei, Y. Du, X.-T. Wu, Q. Xu, R. Zou
10 and Q.-L. Zhu, *Appl. Catal. B: Environ.*, 2021, **283**, 119591.
- 11 33. C.-Z. Yuan, K. Liang, X.-M. Xia, Z. K. Yang, Y.-F. Jiang, T. Zhao, C. Lin, T.-Y. Cheang,
12 S.-L. Zhong and A.-W. Xu, *Catal. Sci. Technol.*, 2019, **9**, 3669-3674.
- 13 34. X. Yang, J. Cheng, B. Fang, X. Xuan, N. Liu, X. Yang and J. Zhou, *Nanoscale*, 2020, **12**,
14 18437-18445.
- 15 35. K. Jiang, S. Siahrostami, T. Zheng, Y. Hu, S. Hwang, E. Stavitski, Y. Peng, J. Dynes, M.
16 Gangisetty, D. Su, K. Attenkofer and H. Wang, *Energy Environ. Sci.*, 2018, **11**, 893-903.
- 17 36. C. F. Wen, F. Mao, Y. Liu, X. Y. Zhang, H. Q. Fu, L. R. Zheng, P. F. Liu and H. G. Yang,
18 *ACS Catal.*, 2020, **10**, 1086-1093.
- 19 37. X. Rong, H.-J. Wang, X.-L. Lu, R. Si and T.-B. Lu, *Angew. Chem. Int. Ed.*, 2020, **59**,
20 1961-1965.
- 21 38. Q. He, D. Liu, J. H. Lee, Y. Liu, Z. Xie, S. Hwang, S. Kattel, L. Song and J. G. Chen,
22 *Angew. Chem. Int. Ed.*, 2020, **59**, 3033-3037.
- 23 39. W. Ren, X. Tan, W. Yang, C. Jia, S. Xu, K. Wang, S. C. Smith and C. Zhao, *Angew. Chem.
24 Int. Ed.*, 2019, **58**, 6972-6976.
- 25 40. M. Zhang, Z. Hu, L. Gu, Q. Zhang, L. Zhang, Q. Song, W. Zhou and S. Hu, *Nano Res.*,
26 2020, **13**, 3206-3211.
- 27 41. C. Ding, C. Feng, Y. Mei, F. Liu, H. Wang, M. Dupuis and C. Li, *Appl. Catal. B: Environ.*
28 2020, **268**, 118391.
- 29 42. W. Zhu, L. Zhang, S. Liu, A. Li, X. Yuan, C. Hu, G. Zhang, W. Deng, K. Zang, J. Luo, Y.
30 Zhu, M. Gu, Z.-J. Zhao and J. Gong, *Angew. Chem. Int. Ed.*, 2020, **59**, 12664-12668.
- 31 43. J. Pei, T. Wang, R. Sui, X. Zhang, D. Zhou, F. Qin, X. Zhao, Q. Liu, W. Yan, J. Dong, L.
32 Zheng, A. Li, J. Mao, W. Zhu, W. Chen and Z. Zhuang, *Energy Environ. Sci.*, 2021, DOI:
33 10.1039/D0EE03947K.
- 34